

JULIUS-MAXIMILIANS-UNIVERSITÄT-WÜRZBURG

BACHELOR THESIS

---

# Measuring Brightness Temperature Gradients in Extragalactic Jets

---

*Author:*

Paul Ray Burd

*Supervisor:*

Prof. Dr. Matthias Kadler



*A thesis submitted in fulfilment of the requirements  
for the degree of Bachelor of Science*

*in the group of*

Prof. Dr. Matthias Kadler  
Department for Astrophysics



# Contents

<b>Abstract</b>	<b>3</b>
<b>1 Active Galactic Nuclei</b>	<b>5</b>
1.1 Emission Lines from AGN . . . . .	5
1.2 Radio Loud and Radio Quiet Galaxies . . . . .	6
1.3 Blazars . . . . .	6
1.3.1 BL Lacertae . . . . .	7
1.3.2 Quasars . . . . .	7
1.4 Unification Model . . . . .	7
<b>2 Jet Models</b>	<b>11</b>
2.1 Synchrotron Radiation . . . . .	12
2.2 Inverse Compton Scattering . . . . .	13
2.3 Observed Flux Density of an Unresolved Jet . . . . .	13
2.4 Brightness Temperature . . . . .	15
<b>3 Sample Selection and Data Reduction</b>	<b>17</b>
3.1 Observations with Radio Interferometry . . . . .	17
3.2 Sample Selection . . . . .	21
3.3 DIFMAP-Model Fitting . . . . .	22
<b>4 Results of the Brightness Temperature Study</b>	<b>29</b>
4.1 1101+384 (Mrk 421) . . . . .	30
4.2 Power Laws with additional Brightness Temperature Excess . . . . .	30
0133+476 . . . . .	31
1652+398 (Mrk501) . . . . .	31
4.3 Conclusion and Outlook . . . . .	32
<b>List of Figures</b>	<b>33</b>
<b>List of Tables</b>	<b>47</b>
<b>Bibliography</b>	<b>49</b>
<b>Acknowledgements</b>	<b>52</b>
<b>A Appendix</b>	<b>55</b>



# Zusammenfassung

Aufgrund der extremen Natur aktiver Galaxienkerne, welche sich in allen Eigenschaften derer widerspiegelt, sind jene in vielen Studien von höchstem astrophysikalischem Interesse. Die Strahlungsprozesse dieser können im gesamten elektromagnetischen Spektrum beobachtet werden. Die größten räumlichen Ausdehnungen der Teilchenjets (Jets) aktiver Galaxienkerne, liegen in der Größenordnung von Megaparsec. Diese erreichen hoch relativistische Geschwindigkeiten. Ende 1970 und Anfang 1980 wurden für derartige Jets, Modelle von [Blandford & Königl \(1979\)](#) und [Königl \(1981\)](#) etabliert.

In der Studie für meine Bachelor Arbeit untersuche ich die Helligkeitstemperaturgradienten für 21 ausgewählte Quellen aus der MOJAVE Datenbank [Lister et al. \(2009\)](#) um die etablierten Modelle anhand von Beobachtungen zu überprüfen. Dabei studiere ich 19 Quasare und 2 BL Lac Objekte. Für jede dieser Quellen werden die Emissionsregionen mit DIFMAP, einem interaktiven Programm zur Erstellung und Synthese von Residuenkarten von Radiointerferometern, durch elliptische Gaußfunktionen modelliert. Basierend auf den Jetmodellen und Annahmen der oben genannten Veröffentlichungen, werden die durch DIFMAP erzeugten Modelle verwendet, um die Helligkeitstemperaturgradienten entlang der Jetachse zu berechnen und modellieren. Aufgrund der Modelle, unterliegen diese Gradienten bestimmten Einschränkungen, welche mit dem Ergebnis einer Helligkeitstemperaturstudie von [Kadler et al. \(2004\)](#), berechnet werden können. Nach diesen Ergebnissen sollte ein Potenzgesetz  $T_b \propto r^s$  die Daten hinreichend beschreiben. Die Ergebnisse meiner Modelle werden mit den erwarteten Werten vom Potenzindex  $s$  verglichen. Da der Index  $s$  vom Skalenverhalten des Spektralindex, des magnetischen Feldes, dem Jetdurchmesser und der Elektronenenergiedichte entlang der Jetachse, abhängt, werden Spektralindex und Polarisationskarten hinzugefügt, um mögliche Abweichungen zu erklären, die sich in Temperaturexzessen in Quellen wie 1652+398 bemerkbar machen. Acht der Quellen lassen sich mit einem einfachen Potenzgesetz beschreiben. Der Index  $s$  der Quelle 0106+013 folgt den Einschränkungen von [Blandford & Königl \(1979\)](#), während 0224+671, 0122-003 und 1102+348 durch die Erweiterungen von [Königl \(1981\)](#) beschrieben werden können. 0133+476, 0333+321 und 1652+398 weisen signifikante Helligkeitstemperaturexzesse auf, was darauf hinweist, dass die Jetmodelle zumindest erweitert werden müssen. Der Mittelwert der Potenzindizes für Quasare ist  $s_{\text{Qasar}} = 2.11 \pm 0.21$ , der für BL Lacs ist  $s_{\text{BLLac}} = 1.77 \pm 0.27$ . Diese stimmen im Rahmen ihrer Fehler überein. Die Überlappung ist jedoch mit einem Wert von 0.07 derart gering, dass weitere Studien systematische Unterschiede in den Helligkeitstemperaturgradienten zwischen Quasaren und BL Lacs zeigen könnten.

# *Abstract*

Active Galactic Nuclei (AGN) are of highly astrophysical interest due to their extreme nature which become manifest in many different ways. The radiative processes of such jets can be observed through the whole electromagnetic spectrum. They show spatial extensions of kilo to mega parsec scales. In the late 1970s and early 1980s [Blandford & Königl \(1979\)](#) and [Königl \(1981\)](#) established models for the highly relativistic particle jets from such AGN.

In my Bachelor Thesis I study the brightness temperature gradients along the jet axis for 21 chosen sources from the MOJAVE data base [Lister et al. \(2009\)](#) to test whether these models are sufficiently predicting the observed behaviour. I chose 19 quasars and two BL Lac objects without bias to check if the jet models generally describe the observations. For each of these sources the synchrotron radiating components are fitted into each epoch for the corresponding source. The components are fitted as elliptical Gaussians. This is accomplished with DIFMAP, an interactive program for synthesis imaging from radio interferometer arrays. The fitted components for each epoch of a source are taken to compute and fit the brightness temperature gradient along the jet axis based on the jet models and assumptions of the mentioned papers. According to those, the expected power law index of the brightness temperature gradient  $s$  follows very specific restrictions which can be calculated by using the results of a brightness temperature study accomplished by [Kadler et al. \(2004\)](#). From these models a simple power law  $T_b \propto r^s$  fit should be applicable to the brightness temperature data.

The results of my model fits are compared with the expected restrictions and values for the power law indices  $s$  for my concerned sources. Since the power law index  $s$  of the brightness temperature gradient depends on the scaling of the spectral index, magnetic field, the jet diameter and the electron energy density along the jet axis I added spectral index maps and polarization maps to describe occurring differences from the model which show up as brightness temperature excesses for some sources like 1652+398.

The main result from this study is that eight of the sources can be fitted as a power law with respect to the brightness temperature gradient along the jet axis. 0106+013 follows the restrictions for the index  $s$  of [Blandford & Königl \(1979\)](#), while 0224+671, 0122-003 and 1101+348 can sufficiently be described by the extensions of [Königl \(1981\)](#). 0133+476, 0333+321 and 1652+398 show a significant brightness temperature excess which suggests that the models for radio jets are to be extended. The mean value for the power law index of the brightness temperature gradient for Quasars  $s_{\text{Quasar}} = 2.11 \pm 0.21$  and BL Lacs  $s_{\text{BL Lac}} = 1.77 \pm 0.27$  show within the interval of the error no significant difference. Since the overlap of the errors is very small 0.14, there might be a systematic difference between Quasars and BL Lacs which has to be studied on a grater sample.

# Chapter 1

## Active Galactic Nuclei

Active galactic nuclei (AGN) are among the most luminous objects in universe which can be seen as broadband emitters. Therefore, an understanding of phenomena related to AGN require multi wavelength observations. According to [Shakura & Sunyaev \(1973\)](#) the most probable form to reach the energies emitted by AGN is the forming of an accretion disc of charged particles around the black hole. Studies published by [Peterson et al. \(2004\)](#) which are based on the dependence of the luminosity of AGN and the central super massive black hole, reveal the luminosity of such objects ranges between  $10^{42} \frac{\text{erg}}{\text{s}} < L \leq 10^{47} \frac{\text{erg}}{\text{s}}$ . The masses of the black holes which are considered as the central machine of AGN, and thus of Quasars, typically are  $10^7 \lesssim \log(M/M_{\odot}) \lesssim 10^{10}$  [Vestergaard & Peterson \(2006\)](#).

The draft description of the AGN, used in this thesis, follows the argumentation and descriptions of [Robson \(1996\)](#).

### 1.1 Emission Lines from AGN

There are two types of emission lines which are used to distinguish AGN, the permitted and the forbidden line. Permitted lines are caused by radiative emission. Forbidden lines are seen when a atom de-excites in a low density gas. In a dens gas all energy of the atom is lost due to collisions with other atoms, before forbidden lines can be seen because the rate of reaction for forbidden lines is much lower than the rate for allowed ones. It is important to mention, that forbidden lines also occur in high density gas and are much stronger than in low density gases but as the density reaches a critical value, the emissivity of forbidden lines becomes constant. The emissivity of allowed lines increases linear with the gas density. Due to these facts, the presence of forbidden lines give information about the pressure and density of the medium where the atoms exist.

## 1.2 Radio Loud and Radio Quiet Galaxies

To distinguish radio-quiet and radio-loud sources, [Kellermann et al. \(1969\)](#) introduced the ratio of radio to optical flux. A source is said to be radio loud when

$$R_{r-o} = \frac{S_r}{S_o} \geq 10. \quad (1.1)$$

A source is said to be radio quiet when

$$0.1 < R_{r-o} < 1. \quad (1.2)$$

If a galaxy is radio-loud it indicates that the radiation is non-thermal. This means that this type of radiation is emitted by a highly relativistic particle jet where the particles are accelerated by a magnetic field. Among other radiative processes (such as inverse Compton scattering or pair production), the electrons accelerated and confined by a magnetic field, emit synchrotron radiation which can be detected by radio telescopes. Therefore, a radio-loud galaxy indicates the presence of a jet. The term 'jet' can be defined in the radio regime according to [Bridle & Perley \(1984\)](#) as a radio emission feature which is at least four times long as wide. It should be distinguishable from other extended structures at high resolutions and it is aligned with the compact radio core. In fact when following, the argumentation of [Stoche et al. \(1992\)](#) radio-quiet galaxies also form small jets where the particle's acceleration is sub relativistic and the line widths are much narrower than in radio-loud galaxies. However in a first approximation which is appropriate for this work, it will be assumed that radio-loud galaxies are to be examined when working with extragalactic jets.

## 1.3 Blazars

Following the argumentation of [Antonucci \(1993\)](#), Blazars are core dominated radio sources which show a highly variable, polarized optical spectrum. Historically when the optical spectrum is a featureless continuum these sources are called BL Lacertae objects (BL Lacs). If broad emission lines can be detected these kind of Blazars are called Optically Violently Variable Quasars (OVV's). OVV's are weaker in the radio regime than BL Lacs but stronger in the optical. The third kind of AGN which can be counted to this class are the flat spectrum radio quasars (FSQR) which are more luminous than BL Lacs and show broad emission lines.

### 1.3.1 BL Lacertae

BL Lac here refers to classical radio selected BL Lacs. There are also X-ray selected BL Lacs which show strong X-ray emission and a featureless, with respect to emission lines, optical spectrum. Classical BL Lacs are radio loud in terms of 1.2. They usually are flat spectrum radio sources with a featureless continuum spectrum, following a power law  $F(\nu) \propto \nu^\alpha$  through the entire electromagnetic spectrum, showing a strong variability in terms of luminosity (radio flux) and polarization which is very strong. Emission lines, found in the optical part of the spectrum are red shifted which shows that BL Lacs indeed are extragalactic objects. According to a study of Mrk 501 (1652+398) by [Albert et al. \(2007\)](#) the variation with respect to the observed flux of BL Lacs happen within minutes which indicates the strong variability on short time scales of these objects. Also on time scales like months the flux varies at different observation energies.

### 1.3.2 Quasars

Just like BL Lacs, the flat spectrum of a Quasar follows a power law through the whole electromagnetic continuum. The term Quasar will be used in this study as a FSQR, described in 1.3. Quasars can be subdivided by broad emission lines and narrow emission lines, as Quasar type 1 and type 2. For Quasars especially the emission lines of hydrogen are very strong. The emission lines of a Quasar are similar to the strongest lines of Seyfert 1 galaxies. This can be explained by a broad line region of emitting gas as in the case of Seyfert 1. The variability with respect to flux of quasars happens according to [Ulrich et al. \(1997\)](#) within weeks but also can occur during months. The spectrum is a strong polarized continuum. There are also radio quiet Quasars, called quasi stellar objects but these galaxies will not be considered here.

## 1.4 Unification Model

Taking a closer look at the narrow line radio galaxies (NLRG) and broad line radio galaxies (BLRG), an understanding of a grand unification according to [Antonucci \(1993\)](#) and [Urry & Padovani \(1995\)](#) can be obtained. [Antonucci & Barvainis \(1990\)](#) argued that NLRGs can be interpreted as quasars, which are BLRGs, in the sky plane. This explains the absence of broad emission lines, since the dust torus then would cover the narrow emission line region. In fact there are more hints that such an unification scheme may be accomplished referring to the similarities in emission lines of Seyfert 1 and Quasars but since my work focusses mainly on radio loud sources I concentrate my explanation on NLRGs and BLRGs. The far accepted unification model contains a central super

massive black hole (SMBH) surrounded by an accretion disk. This accretion disc forms depending on the rotation of the black hole and the accretion disc at different distances from the event horizon from the black hole. The accretion disc can form at the innermost stable circular orbit (ISCO). According to [Camenzind \(2007\)](#) the radius of the ISCO can be written in terms of the Kerr parameter  $a$  which describes the angular momentum of the black hole as

$$r_{\text{ISCO}} = 2M \pm a + 2\sqrt{M^2 \pm aM} \quad (1.3)$$

This is written in natural units. Hence the gravitational radius reads  $r_g = M$ . The Kerr parameter ranges between  $-M \leq a \leq M$ . This equation suggests the extremes for  $r_{\text{ISCO}}$ . The first situation, where  $a = 0$  for a non spinning black hole yields  $r_{\text{ISCO}} = 6r_g$ . The case of a retrograde to the accretion disc spinning black hole, where  $a = -M$ , yields  $r_{\text{ISCO}} = 9r_g$ . The limit where  $a \rightarrow M$  has to be dealt in terms of  $a = M(1 - \delta)$  where  $\delta$  is an infinitesimal small displacement from the mass  $M$ . In this case the radius of the stable orbit is  $r_{\text{ISCO}} = r_g(1 + [4\delta]^{1/3})$ . This means for a maximum of the black hole's spin and an accretion disc spinning in the same direction, the  $r_{\text{ISCO}}$  is near the gravitational radius of the black hole. This is explained by frame dragging which will not be discussed here <sup>1</sup>. Additionally a dust cloud formed as a torus and also in the plane of the accretion disc marks the narrow line emission region. At a viewing angle which is perpendicular to the jet axis this torus covers the accretion disc and the broad line emission region. According to [Holt et al. \(1992\)](#) and [Urry & Padovani \(1995\)](#) for a black hole with  $M = 10^8 M_\odot$  the black hole radius is  $r_{\text{BH}} = r_g \approx 1.5 \times 10^{11}$  m, where the gravitational radius reads  $r_g = \frac{MG}{c^2}$ . The accretion disc then emits at a distance  $d$  from the black hole of  $r_g \lesssim d \lesssim 30 r_g$ , the broad line clouds are located within  $2 \times 10^3 r_g \lesssim d \lesssim 20 \times 10^3 r_g$ . The inner radius of the torus is roughly located at  $d \approx 10^4 r_g$  while the narrow line emission region extends to  $10^5 r_g \lesssim d \lesssim 10^7 r_g$ . As an approximation only the radio loud sources are said to have jets as suggested in section 1.2. [Bregman \(1990\)](#) divides AGN into those which are dominated by thermal radiation at the 1 – 1000  $\mu\text{m}$  continuum with temperatures from approximately 40 – 2000 K. For the Blazar class the radio throughout the gamma continuum is dominated by non-thermal radiation. For radio quiet sources the continuum suggests that there are four separate emission components, the radio, submillimeter infra red, near infra red to soft X-ray and the X-ray region. The difference between the types of AGN here is on the one hand the angle under which the AGN is observed. Consider the line of sight being perpendicular to the jet axis, then the dust cloud would cover the broad line region which would then let these emission lines be undetectable. On the other hand AGN can be classified by looking at the luminosity. Seyfert 1 galaxies and radio quiet quasars can be seen under the same angle with respect to the line of sight, but they differ in terms of luminosity. Table 1.1

<sup>1</sup>for further reading on the effects of frame dragging: [Camenzind \(2007\)](#) and [Misner et al. \(1973\)](#)

and figure 1.1 summarize the unification model with its classification by radio loud and quiet and the angular with respect to the line of sight.

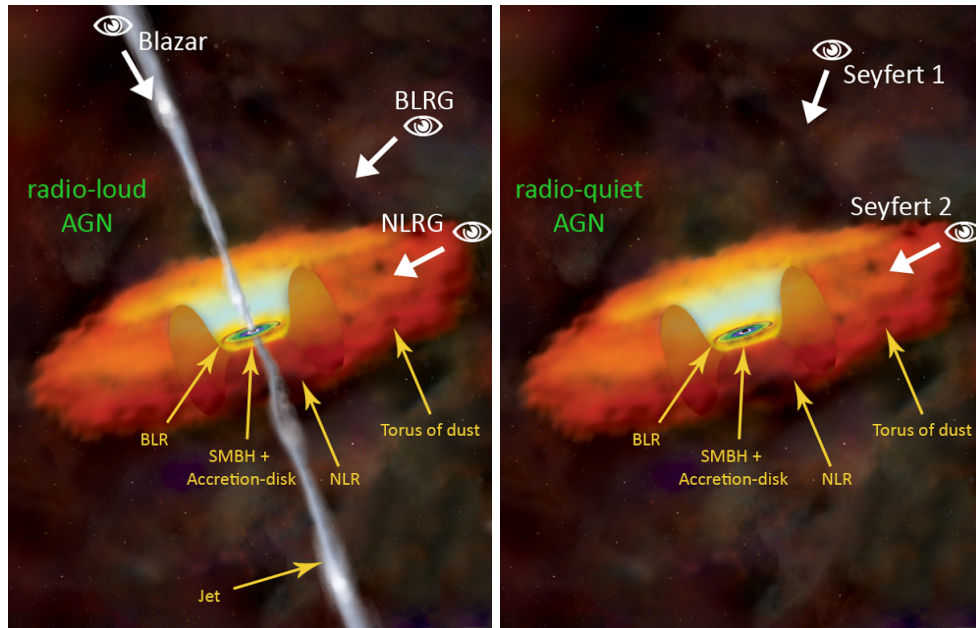


FIGURE 1.1: Visual summary of the unification model based on the summary of [Urry & Padovani \(1995\)](#); At the center is the SMBH surrounded by the accretion disc and the dust torus. On the left picture the radio loud AGN are illustrated, on the right picture the radio quiet AGN are illustrated. Credit: NASA/CXC/M.Weiss; edited by Jonas Trüstedt

TABLE 1.1: Summary of the Unification Model Credit: Matthias Kadler, edited by Paul Ray Burd

Type	Radio Loudness	Emission Lines	Luminosity	Jet	Radio Morphology
Seyfert 1	quiet	broad+narrow	low	none	none
Seyfert 2	quiet	narrow	low	none	none
QSO	quiet	broad+narrow	high	none	none
QSO	quiet	narrow	high	none	none
BLRG	loud	broad+narrow	low	yes	FR1
BLRG	loud	broad+narrow	high	yes	FR2
NLRG	loud	narrow	low	yes	FR1
NLRG	loud	narrow	high	yes	FR2
BL Lac	loud	none	low	yes	compact
FSQR	loud	broad+narrow	high	yes	compact

## Chapter 2

# Jet Models

This study focusses on testing the jet models established by [Blandford & Königl \(1979\)](#) and [Königl \(1981\)](#). To explain the power law dependency of the emitted energy of relativistic electrons, confined and accelerated by a magnetic field, the non thermal synchrotron radiation as an example of radiative losses will be discussed. Another important type of radiative energy losses of electrons is the Inverse Compton scattering. This type of emission dominates the core and the core region. The terminology 'core' refers not to the central SMBH but to the origin of the radio emission, where the optical depth for synchrotron radiation at  $\nu = 15$  GHz is  $\tau \gtrsim 1$ . This effect has to be considered carefully when analysing the brightness temperature gradient plots. The assumptions on which these two papers are based are summarized in the paper of [Königl \(1981\)](#) and are listed in the following:

- a) A narrow conical jet is considered with a semi opening angle  $\phi$  and the angle  $\theta$  under which the jet is observed
- b) The jet has a constant velocity  $\beta_j$ .
- c) The electrons are ejected continuously, where the energy density of the ejected electrons declines as a power law along the jet axis  $n \propto r^n$ .
- d) The magnetic field scales with a power law along the jet axis  $B \propto r^b$ .

The quantity  $r$  in assumption c) and d) is the jet axis.  $n$  describes the electron energy density with respect to the jet axis and  $B$  is the magnetic field. The consequence of these assumptions is a given jet geometry which induces a very specific expected flux. This will be explained in the following sections.

## 2.1 Synchrotron Radiation

Relativistic charged particles radiate when accelerated by a magnetic field. This process is called synchrotron radiation. A derivation for the emitted power of a charged particle in a magnetic field is given by [Rybicki & Lightman \(1979\)](#). It can be described by equation 2.1 which is also called Larmor's formula.

$$P = \frac{dE}{dt} = \frac{q^2 \dot{v}^2}{4\pi c^3} \int \sin^2 \theta d\Omega = \frac{2q^2 \dot{v}^2}{3c^3} \quad (2.1)$$

Equation 2.2 gives the averaged power which is emitted by an electron in a magnetic field under the assumption of an isotropic velocity distribution and a relativistic motion of the electrons.

$$\langle P_{\text{em}} \rangle = \frac{4}{3} \beta^2 \gamma^2 c \sigma_T u_B \quad (2.2)$$

where the Thomson cross section is given by  $\sigma_T = \frac{8\pi e^2}{3m_e^2 c^4}$  and the magnetic field energy density  $u_B = \frac{B^2}{8\pi}$ ;  $\gamma = \left(\sqrt{1 - \beta^2}\right)^{-1}$ , where  $\beta = v/c$ . As the mass of the electron scales with a power of 2 in the denominator of the Thomson cross section, the proportionality in  $P_{\text{em}} \propto m_e^{-2}$  suggests that the synchrotron emission of charged particles with a large mass in first order is negligible. This leptonic model, established by [Blandford & Königl \(1979\)](#) and [Königl \(1981\)](#), was extended by [Mannheim \(1993\)](#) by adding emitting protons as radiative components which induce high energy emission from X-ray to gamma ray, hence [Mannheim \(1993\)](#) extended the existing models to a hadronic model. However in this work I only consider a pure leptonic model. For an electron distribution  $n(\gamma)$  the power of each electron has to be weighted to get a power spectrum.

$$P_\nu = -\frac{dE}{dt} = \int_1^\infty P_\nu(\gamma) n(\gamma) d\gamma \quad (2.3)$$

The most important case is the non thermal synchrotron radiation where electrons appear to follow a power law distribution.

$$n(\gamma) d\gamma = n_0 \gamma^{-p} d\gamma. \quad (2.4)$$

The spectral power distribution can be written in terms of a function  $\Phi_\nu(\gamma)$  which described the spectral shape and is normed to one with respect to the frequency  $\nu$ . Therefore the power distribution is given by

$$P_\nu(\gamma) = \frac{4}{3} \beta^2 \gamma^2 c \sigma_T u_B \Phi_\nu(\gamma) \quad (2.5)$$

The assumption that photons are only emitted at the characteristic frequency  $\omega_c = \frac{eB}{m_e c} \left( \frac{E}{m_e c^2} \right)^2 = \gamma^2 \nu_L$ , where  $\nu_L$  is Larmor's frequency yields a spectral shape function which can be written in terms of a Dirac distribution  $\Phi_\nu(\gamma) \approx \delta(\nu - \omega_c)$ . This is a proper approximation since the emission spectrum of an electron has a strong peak at this frequency. The integral in equation 2.3 then can be calculated to

$$P_\nu = \frac{2}{3} c \sigma_T n_0 \frac{u_B}{\nu_L} \left( \frac{\nu}{\nu_L} \right)^{-\frac{p-1}{2}} \quad (2.6)$$

Here  $\alpha = \frac{p-1}{2}$  is the spectral index thus the emitted power follows also a power law like the particle distribution.

## 2.2 Inverse Compton Scattering

The process of inverse Compton scattering transfers energy of a high relativistic electron to a distribution of photons with very low energy compared to the electron. A derivation for the power for a single scattering event is given by Rybicki & Lightman (1979) and Blumenthal & Gould (1970). In this thesis, however, I will follow the formulation and argumentation of Rees (1967). The energy loss of a high relativistic electron with the energy  $E \gg m_0 c^2$  in a isotropic radiation field with the energy density  $\epsilon_{\text{rad}}(\nu)$  is given by

$$-\frac{dE_c}{dt} = \frac{3}{8} c \sigma_T \int \epsilon_{\text{rad}}(\nu) \left( \frac{m_0 c^2}{h\nu} \right)^2 \log \left( \frac{2Eh\nu}{m_0^2 c^4} + \frac{1}{2} \right) \quad (2.7)$$

$\sigma_T$  is the Thomson cross section,  $h$  is the Planck constant,  $\nu$  is the radiation's frequency and  $E$  is the energy of the scattered photons.  $\epsilon_{\text{rad}}$  is the energy density of the radiation field. It is assumed that nearly all photons have the same energy.

## 2.3 Observed Flux Density of an Unresolved Jet

The observed flux density for an unresolved jet is calculated by Königl (1981). It can be calculated by

$$S_{\text{ob}}(\nu) = \frac{(1+z)D_j^2}{4\pi D_l^2} \int_{r_M}^{r_u} \epsilon_s \left( \frac{(1+z)\nu}{D_j} \right) \pi(r\phi)^2 dr \quad (2.8)$$

where  $D_j = \frac{1}{\gamma_j(1-\beta_j \cos\theta)}$  is the Doppler factor which takes into account that the emission from the jet is boosted in the  $\theta$  direction. The luminosity distance  $D_l$  is measured in parsec. The redshift is  $z$  and  $\epsilon$  is the emissivity of the considered radiation. Equation

2.8 can now be used to calculate the synchrotron spectrum of a jet. The emissivity for synchrotron radiation is given by

$$\epsilon_s \left( \frac{(1+z)\nu_s}{D_j} \right) = (1+z)^\alpha D_j^{-\alpha} \nu_s^\alpha C_1(\alpha) n_e B^{1-\alpha} \quad (2.9)$$

where  $C_1(\alpha)$  is a constant which is specific for a considered spectral index at one parsec from the core. These constants are calculated by [Blumenthal & Gould \(1970\)](#). The limit  $r_M$  is the smallest distance from the core at which optically thin synchrotron emission can be observed while  $\nu_{\text{SM}}$  is the frequency of the radiation at this distance.

$$r_M \approx \left( 1.6 \times 10^6 D_j^{-1} (\gamma_j \beta_j)^{-6} K_1 B_1^{11} \phi \csc(\theta) \right)^{-1/(11b+n+7)} \text{ pc} \quad (2.10)$$

For  $\alpha = -0.5$ , the frequency at  $r_M$  is given by

$$\nu_{\text{SM}} \approx 6.9 \times 10^7 (1+z)^{-1} \times \left( (1.6 \times 10^6 K_1 \phi \csc(\theta))^{-(3b+2)} D_j^{-(8b+n+5)} (\gamma_j \beta_j)^{-(4b+2n+2)} B_1^{3n-1} \right)^{-1/(11b+n+7)} \text{ Hz} \quad (2.11)$$

The quantities  $K_1$  and  $B_1$  refer to the injected electrons and the magnetic field at 1 pc distance from the SMBH.  $r_u$  is the distance where the synchrotron spectrum terminates. By using 2.8 and 2.9 [Königl \(1981\)](#) calculated the observed flux density for the synchrotron spectrum of the jet as

$$S_{\text{obs } s}(\nu_s) = \begin{cases} S_{\text{obs } s}(\nu_{\text{SM}}) (\nu_s / \nu_{\text{SM}})^{\alpha_{s1}}, & \nu_{\text{SM}}(r_u / r_M)^{-k_m} \lesssim \nu_s \leq \nu_{\text{SM}} \\ S_{\text{obs } s}(\nu_{\text{SM}}) (\nu_s / \nu_{\text{SM}})^{\alpha_{s2}}, & \nu_{\text{SM}} \lesssim \nu_s \leq \nu_{\text{SM}}(r_u / r_M)^{k_b} \end{cases} \quad (2.12)$$

Calculating equation 2.12 with the frequency from equation 2.10 gives

$$S_{\text{obs } s}(\nu_{\text{SM}}) \approx 3 \times 10^4 \frac{C_1(-\alpha)}{C_1(-0.5)} (1+z)^{1+\alpha} D_l^{-2} D_j^{2-\alpha} \phi^2 K_1 B_1^{1-\alpha} \nu_{\text{SM}}^{+\alpha} \frac{r_M^{-k_s}}{k_s} \text{ Jy} \quad (2.13)$$

where  $k_s = -[(1-\alpha)b + n + 3]$ . For the optical thin synchrotron emission the spectral index is  $\alpha_s = \alpha + 0.5$ , where  $\alpha$  is the spectral index of the injected electrons. The power law indices  $k_b = -(3b + 2)$  and  $k_m = ((3 - 2\alpha)b + 2n + 2)/(2\alpha - 5)$  are calculated by the power law index  $n$  with which the electron energy density scales along the jet axis, the index  $b$  which gives information about the behaviour of the magnetic field and the spectral index of the injected electrons  $\alpha$ . These indices can be used to calculate the spectral indices  $\alpha_{s1} = (4 - b - 5k_m)/2k_m$   $\alpha_{s2} = -(\alpha + k_s)/k_b$  where  $k_s = -[(1-\alpha)b + n + 3]$ . These two spectral indices also take the non uniformity of the jet in the optical thick and the optical thin region into consideration. Equation 2.12 can be used to predict the behaviour of the flux density at different point in the jet.

## 2.4 Brightness Temperature

In a study of fine scale structures of Quasars, which means that structures in the regime of milliarcseconds are investigated, [Kovalev et al. \(2005\)](#) gave a formula for the brightness temperature.

$$T_b = \frac{2 \ln 2}{\pi k_b} \frac{S_{\text{core}} \lambda^2 (1+z)}{a_{\text{min}} a_{\text{maj}}} \quad (2.14)$$

$S_{\text{core}}$  is the flux density of the radio emission core and  $\lambda$  is the wavelength of observation which for my studies is  $\lambda = 2$  cm. The quantities  $a_{\text{min}}$  and  $a_{\text{maj}}$  are the FWHMs of the elliptical Gaussian components along the major and minor axes. From that [Kadler et al. \(2004\)](#) gave a dependency of the brightness temperature gradient along the jet axis which follows a power law.

$$T_b \propto r^s \quad \text{and} \quad s = l + n + b(1 - \alpha_s) \quad (2.15)$$

Following proportionalities give the scale behaviour of these quantities

$$\begin{aligned} d &\propto r^l \\ n_e &\propto r^n \\ B &\propto r^b \end{aligned} \quad (2.16)$$

The index  $b$  gives the scale behaviour of the magnetic field along the jet axis  $r$ . The permissible values for this index are seen in table 2.1. Also the spectral index  $\alpha = -0.5$  as given in [Blandford & Königl \(1979\)](#) is the spectral index for the initially injected electrons. [Königl \(1981\)](#) takes into account that different areas in the jet are reigned by different spectral indices. The restrictions he made are also seen in table 2.1. The index  $l$  which describes the jet diameter along the jet axis is held by both papers constant  $l = 1$ . This ensures that the assumption of a narrow conical jet geometry is maintained. The parameter  $n$  which scales the electron energy density along the jet axis can according to [Königl \(1981\)](#) be deduced by the configuration of the magnetic field for a assumed spectral index of  $\alpha = -0.5$ , where  $\alpha$  is the spectral index of the injected electrons, by  $n = \frac{17-7m}{5}$ . From these considerations table 2.1 summarizes the canonical values which would be expected for an extended radio jet for the given parameters. When plotting the brightness temperature gradients with respect to the jet axis single components have compared to most components have brightness temperatures up to  $10^{15}$  K. Precluding fitting mistakes and taking into account that such temperature are measured near the core an explanation for such components according to [Kellermann et al. \(1969\)](#) is the inverse Compton catastrophe. The inverse Compton catastrophe gives an upper limit

for the brightness temperature which can be considered as synchrotron radiation. Inverse Compton catastrophe is based on the assumption that the ratio of the radiation's intensity of inverse Compton scattering ( $L_{IC}$ ) and the intensity of synchrotron emission ( $L_S$ ) is the same as the ratio of the energy density of the radiation field and the magnetic field. According to [Kellermann et al. \(1969\)](#) this can be written in terms of a maximum brightness temperature.

$$\frac{L_{IC}}{L_S} = \frac{u_{rad}}{u_B} \propto \frac{1}{2} \left( \frac{T_{max}}{10^{12}} \right)^5 \nu_C + \frac{1}{4} \left( \left( \frac{T_{max}}{10^{12}} \right)^5 \nu_C \right)^2 \quad (2.17)$$

where  $\nu_C$  is the upper cutoff frequency. For the frequency  $\nu_C \propto 10^{5\pm 1}$  (the unit is MHz), the brightness temperature becomes  $T_{max} \leq 10^{11}$  K. For  $T_{max} \geq 10^{12}$  K the inverse Compton losses become catastrophic according to [Readhead \(1994\)](#) in the sense that they happen rapidly within days. Then the brightness temperature decreases between  $10^{11}$  K  $\leq T_b \leq 10^{12}$  K. Hence the inverse Compton losses become the same as the synchrotron losses so that the ratio of equation 2.16 becomes one. This then is called equipartition. Equipartition is a state which holds on larger time scales than inverse Compton catastrophe. As an example [Kellermann et al. \(1969\)](#) points out that if the maximum brightness temperature occurs at 1 GHz, the half life time of electrons at  $T_{max} \approx 10^{11}$  K is at a scale of about  $10^4$  years. At  $T_{max} \gtrsim 10^{12}$  K the half life time becomes less than one day.

TABLE 2.1: Canonical Values for the power indices from equation 2.15 based on the assumptions given at the beginning of chapter 2 with the restrictions of [Blandford & Königl \(1979\)](#) and [Königl \(1981\)](#)

Power Law Index	<a href="#">Blandford &amp; Königl (1979)</a>	<a href="#">Königl (1981)</a>
$b$	-1	$-1 \geq b \geq -2$
$\alpha$	-0.5	$0 \geq \alpha \geq -1$
$n$	-2	$-0.6 \geq n \geq -2$
$l$	1	1
$s$	-2.5	$-1.4 \geq s \geq -3$

## Chapter 3

# Sample Selection and Data Reduction

In this chapter the data which are used to study the brightness temperature gradients are presented. A brief concept of the technique of radio interferometry will be given to explain the functionality of the very long baseline interferometry (VLBI). The monitoring program MOJAVE<sup>1</sup> from which the data are taken will also be presented. Additionally each source I have selected will be presented by a stacked image over all monitored epochs. The last section in this chapter will consider the model fitting which is done with DIFMAP<sup>2</sup>. Here the model components of each jet are fitted with elliptical gaussians. This method will be shown on the example of 1652+398 for the epoch 2009-01-07.

### 3.1 Observations with Radio Interferometry

The explanations and descriptions concerning interferometry follow [Thompson et al. \(1986\)](#). For a single dish telescope the angular resolution  $\Theta$  is given by the Rayleigh criterion. It can be approximated by equation 3.1, where  $\lambda$  is the wavelength at which a source is observed and  $D$  is the diameter of the radio dish. Since the intensity distribution of an incoming signal can be computed by a Bessel's function, according to [Bass et al. \(1995\)](#), the numerical factor 1.22 is an approximation of the first Bessel's function becoming zero. As the wavelength for an observation is set constant for one observation there is only one way of improving the angular resolution. The diameter of the telescope  $D$  has to be increased which can be done by enlarging the size of the radio telescope. The constraints of this solution are quite obvious since the largest movable

---

<sup>1</sup><http://www.physics.purdue.edu/astro/MOJAVE/index.html>

<sup>2</sup><ftp://ftp.astro.caltech.edu/pub/difmap/difmap.html>

radio telescopes have a diameter of about one hundred meter<sup>3</sup>. The other solution is radio interferometry which is the synchronization of multiple radio telescopes to simultaneously observe an object. The baseline between the telescopes is tried to be arranged as large as possible. This increase of the baseline  $\vec{b}$  improves the angular resolution of the telescope dramatically. This is equivalent with an enlargement of the diameter  $D$  of a single dish. To achieve the best angular resolutions very long baselines are realized in the very long baseline interferometry (VLBI).

$$\Theta \approx 1.22 \frac{\lambda}{D}; [\Theta] = \text{rad} \quad (3.1)$$

The improvement of the angular resolution with the VLBI technology becomes clear when calculating equation 3.1 for the radio telescope in Effelsberg with a dish diameter of  $D = 100$  m and the largest baseline of the MOJAVE interferometer which is about  $b = 8600$  km at a observation wavelength of  $\lambda = 2$  cm. The angular resolutions then are  $\Theta_{\text{Effelsberg}} \approx 50.33$  arcsecs and  $\Theta_{\text{MOJAVE}} \approx 0.59$  milliarcsec which is an improvement of about five orders of magnitude. The basic concept of radio interferometry is explained by an example of a two element interferometer following the concept of [Burke & Graham-Smith \(2009\)](#). Figure 3.1 a) shows the basic concept of a two element interferometer. Two identical telescopes point at a source under the direction  $\vec{s} = \vec{s}_0 + \vec{\sigma}$ , connected by a baseline  $\vec{b}_\lambda$  at the phase centre of the antennas. In the case where  $\tau_g = \tau_i$ , the reference direction  $\vec{s}_0$  is called the phase tracking center.  $\sigma$  is the distance from the center of the source to the center of the primary beam which can be seen in 3.1 b). The index  $\lambda$  predicates that the baseline is measured in units of wavelength  $\vec{b}_\lambda = \vec{b}/\lambda$ . These two antennas track the source while one is designated as a reference antenna. The signal arrives at the second antenna with a geometrical delay of  $\tau_g = \vec{b}\vec{s}/c$ . The terminology signal refers to an incoming superposition of electromagnetic wave fronts. The power received by one telescope depends on the flux density  $S_\nu$  of the source and the collecting, effective area  $A_{\text{eff}}$  of the dish.

$$P = \int_0^\infty d\nu A_{\text{eff}}(\nu) S(\nu) \quad (3.2)$$

where  $S(\nu) = \int d\Omega B(\nu, \phi, \theta)$   $B(\nu, \phi, \theta)$  is the brightness distribution of the observed sky integrated over the solid angle  $d\Omega$ . The output of an antenna from a observation of a object at a frequency  $\nu$  corresponds to the output noise power of a black body at this frequency. This is called brightness temperature. Using the Rayleigh-Jeans approximation ( $h\nu \ll kT$ ) for Planck's formula, the brightness temperature can be calculated as

$$T_b = \frac{B(\nu, \phi, \theta)c^2}{2k\nu^2} \quad (3.3)$$

---

<sup>3</sup>Radio telescope in Effelsberg ( $D = 100$  m), Green Bank Observatory ( $D = 101$  m)

To equalize the signals, the reference antenna is given an instrumental delay  $\tau_i$ . The cross power product  $R_{xy}(\tau)$  over two amplitudes is given by the time average of those  $x(t) = \nu_1 \cos(2\pi\nu t)$  with  $y(t - \tau) = \nu_2 \cos(2\pi\nu(t - \tau))$ , delayed by  $\tau$

$$R_{xy}(\tau) := \langle x(t)y(t - \tau) \rangle = SA(\vec{s})\cos(2\pi\nu\tau_g) = SA(\vec{s})\cos(2\pi\vec{b}_\lambda\vec{s}). \quad (3.4)$$

$S$  is the flux of the source and  $A(\vec{s})$  is the effective area of the antenna. Figure 3.1 illustrates the geometrical quantities which are important when concerning the respond of a two element interferometer to a extended source. The complex visibility function of a source the brightness  $B_\nu(\vec{s})$  where the antenna responds to with an solid angle of  $d\Omega$  is given by

$$V = \int A(\vec{\sigma})B_\nu(\vec{\sigma})\exp(i2\pi\vec{b}\vec{\sigma})d\Omega. \quad (3.5)$$

According to figure 3.1 c) the  $(u, v)$ -plane of a source is introduced, where  $(u, v, w)$  is the rectilinear coordinate system for which  $\vec{s}_0$  defines the  $w$  direction which is perpendicular to the  $(u, v)$ - plane. The offset vector  $\sigma$  is parallel to the  $(u, v)$ -plane.  $u$  is projected in the easterly and  $v$  in the northern direction. The quantities  $l, m, n$  are defined as the direction cosines of the vector  $\vec{s}$ . The coordinates of  $\vec{\sigma}$  then are  $(l, m)$ .  $\vec{s}_0$  is perpendicular to the  $uv$ -plane hence  $w = 0$ . The solid angle then reads  $\Omega = dl dm / \sqrt{1 - l^2 - m^2}$ . The visibility function then reads

$$V = \int_{4\pi} A(l, m)B_\nu(l, m)\exp(i2\pi(ul + vm))\frac{dl dm}{\sqrt{1 - l^2 - m^2}} \quad (3.6)$$

The visibility in the  $(u, v)$ -plane is the Fourier transformed of a source's brightness in the  $(x, y)$ -plane. The limitations of VLBI are the impossibility to cover the entire  $(u, v)$ -plane but only a sample coverage. These missing spaces in the  $(u, v)$ -plane imply a loss of Fourier components in the synthesized image. To counteract this, the observed source is monitored at different times which implies that each pair of telescopes samples a trajectory of spatial frequencies as functions of time. Thus the Earth's rotation is used to cover the empty areas in the  $(u, v)$ -plane. This is called Earth rotation or aperture synthesis. In figure 3.2 the  $(u, v)$ -plane coverage of the MERLIN interferometer array is illustrated while using six telescopes at a observation time of eight hours at different declinations. It is obvious that earth rotation synthesis enhances the coverage dramatically.

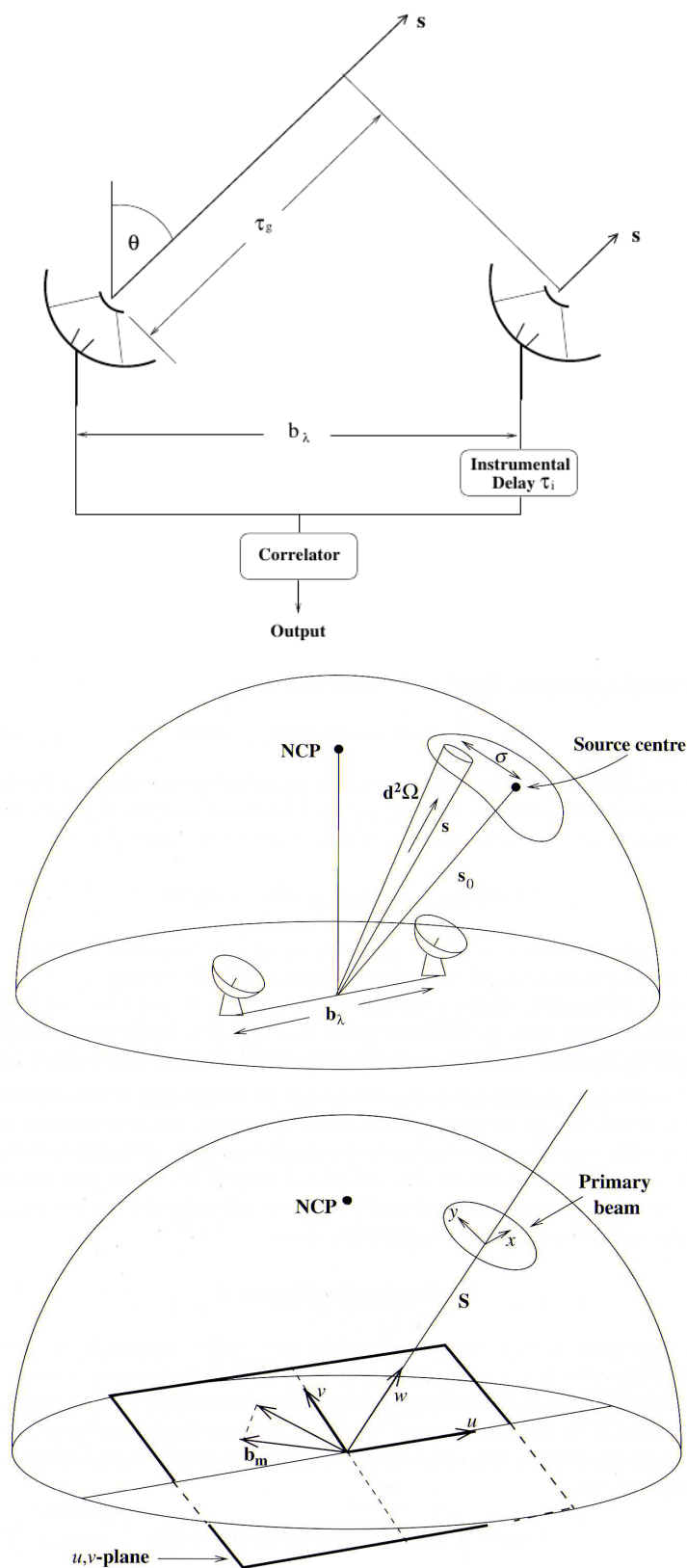


FIGURE 3.1: a) basic concept of a two element interferometer;b) illustrates the receiving element in the direction  $\vec{s}$  and solid angle  $d^2\Omega$  for an extended source; c) introduction of the  $uv$ -plane in relation to the celestial sphere with the North Celestial Pole (NCP);  $x$  and  $y$  are the components of the offset  $\sigma$ ; Credit: [Burke & Graham-Smith \(2009\)](#)

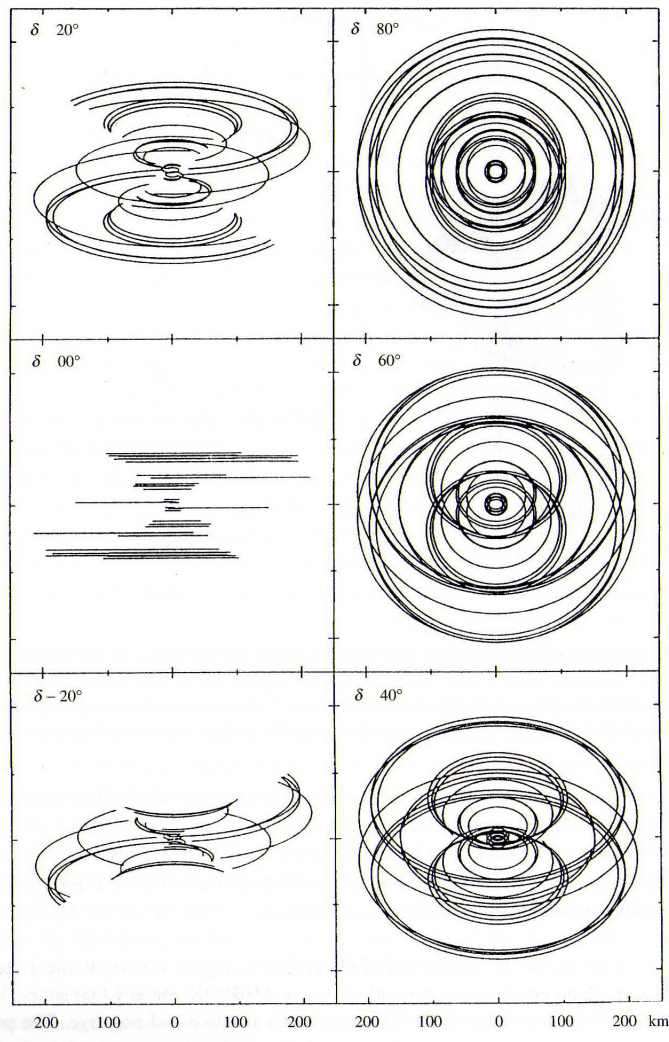


FIGURE 3.2: The  $(u, v)$ -plane coverage of the MERLIN interferometer array is illustrated while in use of six telescopes at a observation time of 8 hours at different declinations  $\delta$ ; Credit: [Burke & Graham-Smith \(2009\)](#)

### 3.2 Sample Selection

MOJAVE (Monitoring Of Jets in Active galactic nuclei with VLBA Experiments) is a monitoring program which continuously observes the radio brightness and polarization variations in jets at  $\lambda = 2$  cm. These jets are associated with AGN which are visible in the northern hemisphere. The observations are made with the high resolution telescope Very Long Baseline Array<sup>4</sup> (VLBA). VLBA is a interferometer build up of 10 telescopes where each dish has a diameter of  $D = 25$  m. The largest baseline between two telescopes in this configuration is between Mauna Kea on Hawaii and St.Croix in the U.S Virgin Islands which is more than 8600 kilometers. This makes it possible to obtain full polarization images with an angular resolution better than 1 milliarcsecond. This

<sup>4</sup><http://www.vlba.nrao.edu/>

research has made use of data from the MOJAVE database that is maintained by the MOJAVE team (Lister et al. (2009)). My selected sources underlie only the bias from MOJAVE itself since I randomly chose the first 19 Quasars and 2 BL Lacs from the MOJAVE data base. From the MOJAVE 1<sup>5</sup> sample, I took 19 Quasars. The MOJAVE 1 sample contains sources for which the declination is greater than  $-30$  degrees, the total VLBA flux density at  $\lambda = 2$  cm exceeds 1.5 at any epoch from 1994 to 2010 and the sources are not associated with gravitational lensing effects. Two BL Lacs, Mrk501 and Mrk421 were taken from the MOJAVE database<sup>6</sup> which were not monitored in the MOJAVE 1 sample. Out of these sources I built up my own sample to test the validity of the jet models established by Blandford & Königl (1979) and Königl (1981) and their restrictions for the quantities described in 2.4. In Tab3.1 the whole sample is given with the AGN classification and the redshift of each source. Furthermore a stacked image of each source will be presented from the MOJAVE web page in figure 3.3. When fitting my sources, two criteria were revealed whether a source's brightness temperature gradient can be studied properly.

- a) the number of fitted components should usually be at least 4<sup>7</sup>
- b) The number of monitored epochs has to be sufficiently large.

There is no sharp cut, whether the number of epochs is sufficiently. It has to be decided for each source separately whether to exclude it because of a lack of epochs. Of course this decision also is based on the number of fitted components.

### 3.3 DIFMAP-Model Fitting

In order to compute a brightness temperature gradient for each source in my sample (3.2) the components of all prevailing sources were fitted into the visibility data taken from the MOJAVE data base. These components were fitted with DIFMAP an interactive program for synthesis imaging from radio interferometer arrays. The components in each epoch were fitted with elliptical Gaussians due to the fact that the fitted emission region is considered to be boosted in a certain direction. An example on 1652+398 (Mrk 501) is given in the following to present the method of model fitting with the epoch from January 7th 2009.

The initial situation is the opened visibility map which can be seen in Fig3.4 a). The red

<sup>5</sup><http://www.physics.purdue.edu/astro/MOJAVE/MOJAVEtable.html>

<sup>6</sup><http://www.physics.purdue.edu/astro/MOJAVE/allsources.html>

<sup>7</sup>further discussion in chapter 3.3; if a source contains many epochs with more than 4 components and only a few with less than four, it is not necessary to exclude these epochs.

TABLE 3.1: Selected Sources with B1950 and common name, AGN classification and redshift

Source (B1950)	Common Name	Redshift	AGN Classification
0016+713	S5 0016+73	1.781 <sup>a</sup>	Quasar
0106+013	4C +01.02	2.099 <sup>b</sup>	Quasar
0109+315	B2 0109+35	0.45 <sup>c</sup>	Quasar
0119+115	PKS 0119+11	0.57 <sup>d</sup>	Quasar
0122-003	UM 321	1.0765 <sup>e</sup>	Quasar
0130-171	OC -150	1.02 <sup>f</sup>	Quasar
0133+476	DA 55	0.859 <sup>a</sup>	Quasar
0202-172	PKS 0202-17	1.739 <sup>g</sup>	Quasar
0202+149	4C +15.05	0.405 <sup>h</sup>	Quasar
0202+319	B2 0202+31	1.466 <sup>i</sup>	Quasar
0212+735	S5 0212+73	2.367 <sup>a</sup>	Quasar
0215+015	OD 026	1.715 <sup>j</sup>	Quasar
0224+671	4C +67.05	0.523 <sup>k</sup>	Quasar
0229+131	4C +13.14	2.059 <sup>l</sup>	Quasar
0234+285	4C +28.07	1.206 <sup>m</sup>	Quasar
0235+164	AO 0235+164	0.94 <sup>n</sup>	Quasar
0241+662	7C 0241+6215	0.045 <sup>o</sup>	Quasar
0333+321	NRAO 140	1.259 <sup>p</sup>	Quasar
0336-019	CTA 26	0.852 <sup>q</sup>	Quasar
1055+018	4C +01.28	0.888 <sup>m</sup>	Quasar
1101+384	Mrk 421	0.0308 <sup>r</sup>	BL Lac
1652+398	Mrk 501	0.0337 <sup>s</sup>	BL Lac

<sup>a</sup> Lawrence et al. (1986)<sup>b</sup> Hewett et al. (1995)<sup>c</sup> Hook et al. (1996)<sup>d</sup> Stickel et al. (1994)<sup>e</sup> Schneider et al. (2002)<sup>f</sup> Wright et al. (1983)<sup>g</sup> Jones et al. (2009)<sup>h</sup> Perlman et al. (1998)<sup>i</sup> Burbidge (1970)<sup>j</sup> Boisse & Bergeron (1988)<sup>k</sup> Sowards-Emmerd et al. (2005)<sup>l</sup> Osmer et al. (1994)<sup>m</sup> Shaw et al. (2012)<sup>n</sup> Cohen et al. (1987)<sup>o</sup> Marziani et al. (2003)<sup>p</sup> Steidel & Sargent (1991)<sup>q</sup> Wills & Lynds (1978)<sup>r</sup> Ulrich et al. (1975)<sup>s</sup> Stickel et al. (1993)

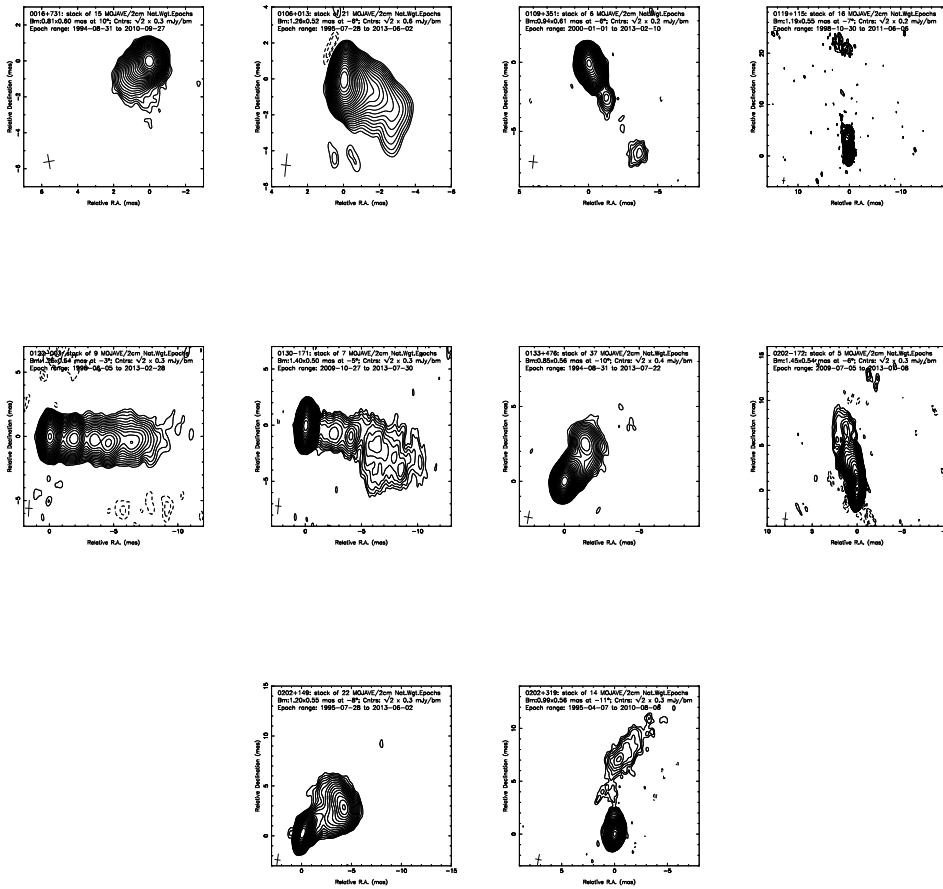


Figure 3.3: For each of my chosen sources a stacked image is given in this figure which means that all imaged epochs are stacked together to obtain an overview of the sources components during the whole observation time span taken from the MOJAVE data base; [Lister et al. \(2009\)](#).

regions in the map contain the flux. In this region a spherical Gaussian component is fitted. The result of the fitting of the first component is given in figure 3.4 b). Again the region with the flux is fitted with a spherical Gaussian to obtain the second component of the jet. The result can be seen in Fig3.4 c). This is an iterative process and it is done until all regions containing flux of the jet are fitted. This iterative process in this case leads to eight fitted components which can be seen in figure 3.4 d). The model components of the clean map 3.4 d) are given in Tab3.2 where the distance of the center of the component from the origin of the plain is given by the radius, the value of the major axis and the axial ratio which for spherical Gaussian of course has the value one. After completing the model fits with spherical Gaussian, the axial ratio is set variable to allow elliptical Gaussian components. The clean map with elliptical Gaussian components can be seen in Fig3.4 e).

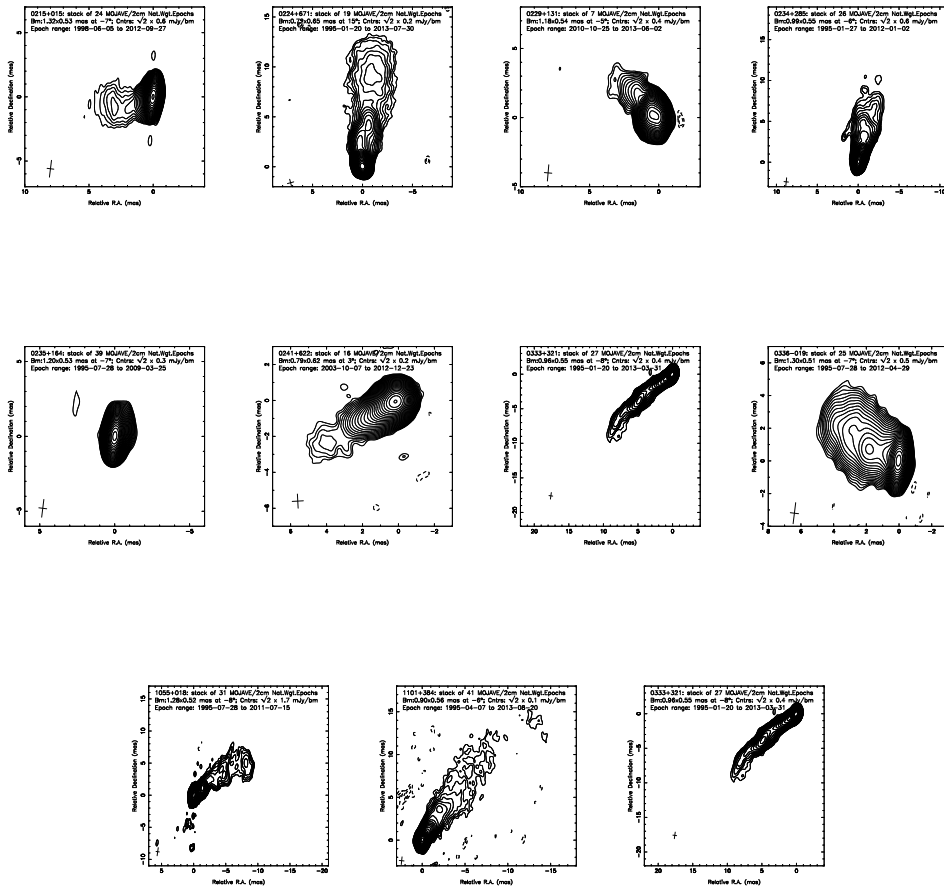


FIGURE 3.3: For each of my chosen sources a stacked image is given in this figure which means that all imaged epochs are stacked together to obtain an overview of the sources components during the whole observation time span taken from the MOJAVE data base; [Lister et al. \(2009\)](#).

According to [Shepherd \(1997\)](#) the terminology clean map refers to a model of the source created by delta functions with the CLEAN deconvolution of the so called dirty map where the model is convolved by elliptical Gaussian approximation of the point spread functions of the interferometer. The dirty map is the Fast Fourier Transformation (FFT) of the  $(u, v)$ -plane.

The model components are listed in [Tab3.3](#). As [Tab3.3](#) suggests, not all components can be calculated as an elliptical Gaussian because the axial ratio would go to zero. Some components have to be kept spherical. Another important thing to mention is that for elliptical components it is more likely that they overlap due to the fact that one single component would contain too much flux which has to be separated into two components which may cause these overlaps.

The core component of the radio emission will be aligned which means that it will be set

into the origin of the  $(u, v)$ -plain. For some epochs it is likely to set the next component after the core component as core region this is often an area where inverse Compton losses are greater than synchrotron losses. Due to this a model can only be considered in terms of a brightness temperature gradient analysis when it contains at least four components. A jet model is treated as an elliptical model when at least one component can be fitted as an elliptical Gaussian.

TABLE 3.2: Spherical Gaussian Components contained in the clean plot of 1652+398 (MRK501) from the epoch 2009-01-07 which is seen in Fig3.4 d); The values for the considered quantities in this table are taken from the DIFMAP log which is created when fitting models into the visibility data

Flux (Jy)	Radius (mas)	Major Axis (mas)	Axial Ratio
0.4503950	0.0303987	0.130325	1.00000
0.0660639	1.0416600	0.679022	1.00000
0.0368679	2.4195800	0.956673	1.00000
0.0538459	8.5172400	2.811400	1.00000
0.0259918	5.3326200	1.715440	1.00000
0.1524250	0.1466430	0.364246	1.00000
0.0134311	11.901200	3.425400	1.00000
0.0287024	3.4709600	0.965022	1.00000

TABLE 3.3: Elliptical Gaussian Components contained in the clean of 1652+398 (MRK501) from the epoch 2009-01-07 which is seen in Fig3.4 e); The values for the considered quantities in this table are taken from the DIFMAP log which is created when fitting models into the visibility data.

Flux (Jy)	Radius (mas)	Major Axis (mas)	Axial Ratio
0.4829050	0.0291507	0.171472	0.555331
0.0594157	1.0747600	0.684173	0.825198
0.0716941	8.4826600	4.430620	0.625328
0.0571120	3.5735800	3.367850	0.306987
0.1233630	0.2053940	0.439957	0.623008
0.0292105	2.6986000	0.989089	1.000000

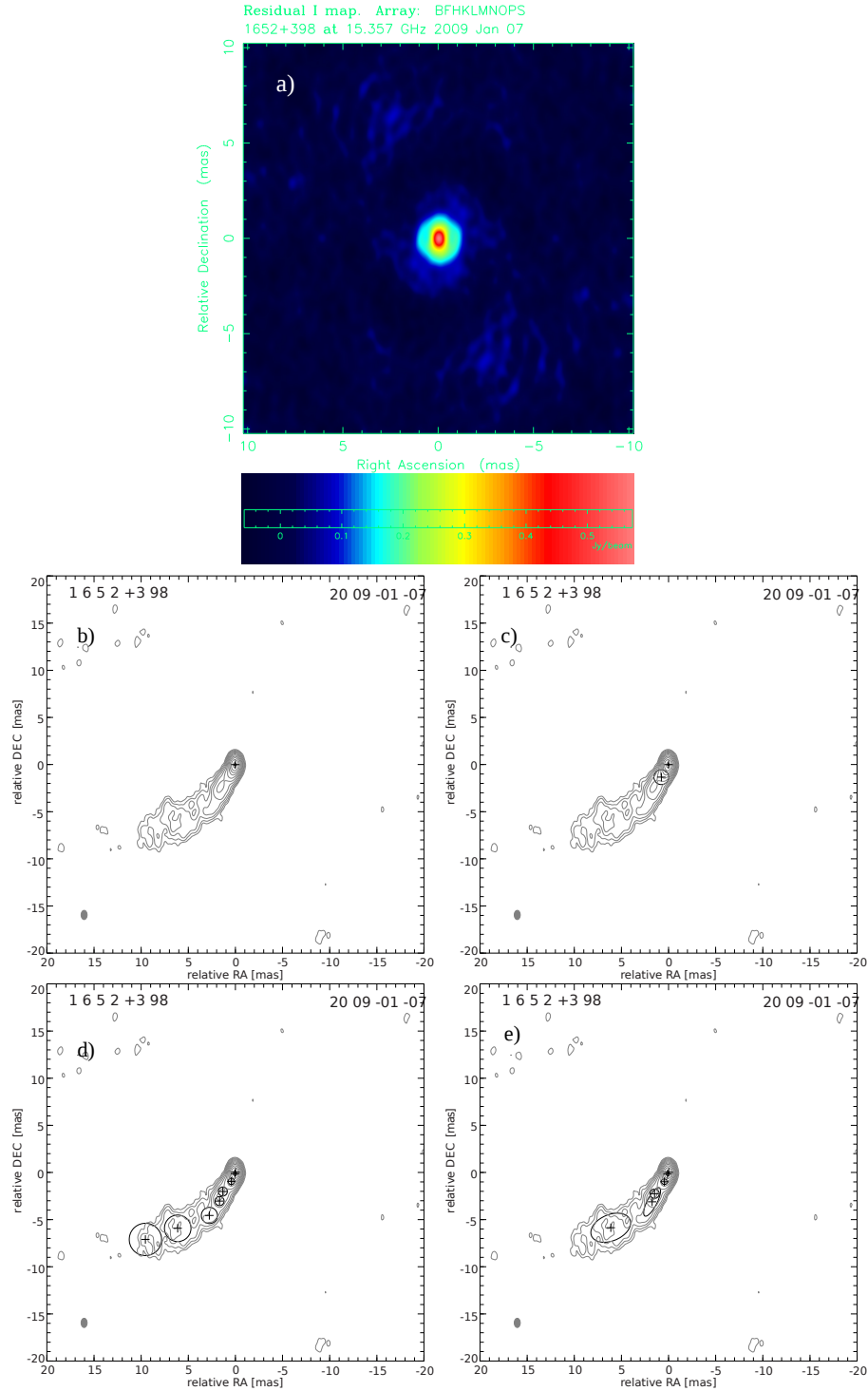


FIGURE 3.4: 1652+398 (Mrk501); epoch 2009-01-07; description will follow from the left top corner to the right bottom corner; a) residual map without component; b) clean map with first component; c) clean map with two components; d) clean map with spherical jet model; e) clean map with elliptical jet model



## Chapter 4

# Results of the Brightness Temperature Study

As described in section 3.2, 21 objects were picked out of the MOJAVE 1 sample and from the MOJAVE data base. They were model fitted as discussed in section 3.3. The following discussions will be done under the assumptions discussed in chapter 2 and with respect to the theories of Blandford & Königl (1979) and Königl (1981) which were adapted to brightness temperature gradients by Kadler et al. (2004).

Each considered source in my sample will be discussed with respect to the fitted brightness temperature power law, the  $\chi^2_{\text{red}}$ , the degrees of freedom (DOF) and the divergences from the expected model. In Tab 4.2 each considered source is listed with a sub classification whether it follows the restrictions of Blandford & Königl (1979) or Königl (1981). Furthermore a power law slope distribution will be presented to find out, if a certain distribution of the values of  $s$  can be determined. There are nine sources out of my sample with 21 sources which were excluded from consideration due to an insufficient number of monitored epochs as discussed in section 3.2. These sources are 0016+713, 0109+351, 0130-171, 0202-172, 0202+319, 0229+131, 0235+164 and 0241+662. Additionally I excluded sources due to an insufficient number of components which were applicable to the uvf due to the reasons which were discussed in section 3.2. These sources are 0119+115, 0202+149, 0215+015 and 1088+018. All excluded sources are Quasars in terms of 1.3.2. Additionally to the excluded ones there are also sources which are considered and can be fitted. However because of the quality of the brightness temperature fits it cannot be said with certainty whether a power law is a valid description for these data. These sources are 0333+321, 0234+285, 0106+013, 0224+671 and 0122-003. Although it is not possible to do certain claims, I will consider these as sources for which a power law is applicable. All considered sources are listed in Tab 4.1. In Tab {tab:sum I present the results of which restrictions the brightness temperature fits follow in terms of Blandford

& Königl (1979) or Königl (1981).

Taking a closer look at the data it can be seen that the brightness temperature for individual components, close to the radio core, is  $T_b \gg 10^{11}$  K. These components have to be concerned as components where catastrophic Inverse Compton losses in terms of 2.4. occur. Hence they are not considered for the fit of the brightness temperature gradient along the jet axis in the regime, where the optical thickness  $\tau < 1$ . Instead these components are treated as the core region, where  $\tau \gg 1$ .

Generally for the brightness temperature fits, a error for the flux is assumed to be 10%. For the minor and major axis of the components, a error of 20% is assumed. The validity of this will also be discussed for each source in the following.

## 4.1 1101+384 (Mrk 421)

In Fig4.1 the fitted power law can be seen for 1101+384. For this source a power law can be fitted without obvious excess or dip. Still the  $\chi_{\text{red}}^2 = 2.98$  with a DOF = 2.98. The divergence from this value to 1 can be explained by an underestimation of the errors, mentioned above. In Tab4.1 different errors for the major and minor axis and the flux are assumed. It turns our that for an error of the flux 20% and a error for the major and minor axis of 30%,  $\chi_{\text{rad}} = 1.2$ . Hence the fitted power law describes the behaviour of the data sufficiently. This source is the only one which can be described with a power law with respect to the brightness temperature gradient along the jet axis.

## 4.2 Power Laws with additional Brightness Temperature Excess

In this section I discuss brightness temperature plots which show a power law behaviour but also, at some regions, predominantly farther away from the core, they show a significant brightness temperature excess. These sources are 0133+476, which is a Quasar in terms of refquasar and 1652+398 (Mrk 501) which is a BL Lac in terms of 1.3.1. A brightness temperature excess can be explained by a variation of any permutation of the power law indices given in equation 2.5. In the following a discussion for each of these sources will be given. Also in this section table 4.2 summarizes with which restrictions the power law index of each source can be described. To explain these excesses one possible explanation among other is the variation of the jet diameter power law index  $l$  is likely to be an explanation for an excess. Both Blandford & Königl (1979) and Königl (1981), consider a narrow conical jet where  $l = 1$ . This model is a vastly simplified perception which indicates that the jet geometry does not change along the jet axis on

sub parsec scales and additionally is not depended on the observed frequency. Further studies in the direction of the frequency dependency of the jet diameter could also reveal a reason for the brightness temperature excesses. The parameter for the electron energy density  $n = (17 - 7b)/5$  couples with the magnetic field power law index  $b$ . To find out whether this influences the power law index  $s$ , theoretical studies need to be done on decoupling these indices. Since for this work I do not have the possibility to study these cases I check whether there is an unusual behaviour of the spectral index based upon the spectral index maps provided by MOJAVE. It is important to mention that these maps are provided for only one epoch for each source so this also can only give a hint for the influence of the spectral index on the parameter  $s$ . In addition detailed polarization maps are needed to check if at the regions of the excesses unexpected things like a change in polarization suggest a variation of the scaling of the magnetic field along the jet axis. The large divergences of  $\Delta\chi^2$  from 1 in this category can of course be explained by the fact, that the brightness temperature excesses cannot be described as simple power laws.

**0133+476** This source is illustrated in Fig 4.2. For  $0.3 \text{ mas} \leq d_{\text{core}} \leq 2.5 \text{ mas}$  this jet follows a power law with respect to its brightness temperature gradient, where the power law index is  $s = -2.145 \pm 0.028$ . At  $2.5 \text{ mas} \leq d_{\text{core}} \leq 3.5 \text{ mas}$  a significant brightness temperature excess can be seen. It is not possible to find an explanation for the excess in the spectral index map for this source. Therefore I chose to include polarization maps<sup>1</sup> for four consecutively epochs from 2011 to 2013 which can be seen in figure 4.9. It is possible to see that the polarization in the region of the excess changes which influences the magnetic field and may cause the brightness temperature excess. It is not possible to do more precise statements since the magnetic field and the electron energy density are still coupled as discussed in 4.2.

The fitted index is  $s = -2.145 \pm 0.028$ , where  $\chi_{\text{red}}^2 = 16.75$  and a  $\text{DOF} = 121$ . These values hold for the plot where the excess is included. Excluding the brightness temperature excess, hence plotting the data only to  $d_{\text{core}} \lesssim 2 \text{ mas}$ , leads to  $s = -2.145 \pm 0.028$   $\chi_{\text{red}}^2 = 7.1$ , where  $\text{DOF} = 73$ . This of course is still not acceptable, but still some possible reasons for the the difference of  $\chi_{\text{red}}^2$  are that the models did not find an absolute minimum. A strong cross-talk between components might introduce scattering which would lead to an underestimation of the errors. Furthermore there are multiple zones in the plot. Beside brightness temperature excess at  $2.5 \text{ mas} \leq d_{\text{core}} \leq 3.5 \text{ mas}$  there is an underlying power law at  $d_{\text{core}} \lesssim 2 \text{ mas}$  which shows dips and excesses.

**1652+398 (Mrk501)** Fig. 4.3 illustrates the brightness temperature data for this source. The fit as it is illustrated leads to  $s = -1.197 \pm 0.020$ ,  $\chi_{\text{red}}^2 = 6.70$  where

<sup>1</sup><http://www.physics.purdue.edu/astro/MOJAVE/sourcepages/0133+476.shtml>

DOF = 109. In a private communication between Till Steinbring and me, he confirmed that there is a break in the power law of the brightness temperature gradient around  $d_{\text{core}} \approx 2$  mm.

Fitting a power law to the data for  $d_{\text{core}} < 2$  mas, leads to  $s = -1.29 \pm 0.07$ ,  $\chi_{\text{red}}^2 = 1.52$  with DOF = 63. The difference of  $\chi_{\text{red}}^2$  from 1 can be explained by a cross-talk between the components which induce scattering and a underestimation of errors. Hence this part of the data can sufficiently be described with an power law.

Fitting a power law to the data for  $d_{\text{core}} \lesssim 2$  mas, hence only excluding the brightness temperature excess, which is explained in terms of 4.2, leads to  $s = -1.172 \pm 0.030$ ,  $\chi_{\text{red}}^2 = 3.05$  with DOF = 129. The difference of  $\chi_{\text{red}}^2$  from 1 can be explained by a cross-talk between the components which induce scattering and a underestimation of errors. Additionally there are dips and excesses which influence the quality of the brightness temperature fit.

### 4.3 Conclusion and Outlook

In table 4.1 each source for which a power law fit with respect to the brightness temperature along the jet axis can be applied is listed with the corresponding power law index, the  $\Delta\chi^2$  and the DOF. In table 4.2 for these sources, a statement whether there is a significant excess of brightness temperature or not and a statement, which restrictions for the index are fulfilled in terms of Blandford & Königl (1979) and Königl (1981) is given.

In figure 4.11 all power law indices for the brightness temperature gradients  $s$  are plotted in a histogram to study the frequency of each class for which the binning is 0.25. The Quasars are marked blue and the BL Lacs red. The plot peaks between 2 and 2.25 suggests a power law behaviour of the brightness temperature gradient according to Königl (1981). This indicates, that the restrictions of Blandford & Königl (1979) might be an oversimplification when describing extragalactic jets properly. Since 1101+284 and 1652+398 are high energy peaked BL Lacs, the question arises whether there is also a systematic difference between these two kinds from the Blazar sequence. Another remarkable thing is a break in the power law fit of the brightness temperature between the frequencies  $\nu = 15$  Ghz and  $\nu = 43$  Ghz. This means that the fitted value for  $s$  differs at different frequencies  $\nu$ . To study the nature of Quasars and BL Lacs, there is an ongoing project at Matthias Kadler's group to enhance the number of considerable sources to find out, whether there is a systematic difference between Quasars and BL Lacs with respect to a brightness temperature study. Also this project concentrates on data, taken at two different frequencies  $\nu = 15$  Ghz and  $\nu = 43$  Ghz to find out if this

break I mentioned before is a property applicable to a significant number of AGN or if it is a source specific phenomenon. It becomes clear that the assumptions which are made in chapter 2 for many cases are a sufficient approximation when describing radio jets. Yet the divergences from these models which were found in this study, especially the brightness temperature excesses show that certain processes concerning the influence of the magnetic field, spectral index, jet diameter and electron energy density are not yet well understood. The excesses of 1652+398 and 0333+321 can be understood by a variation of the spectral index. The excess of 0133+476 otherwise can be explained by a variation of the polarization and thus a variation of the magnetic field along the jet axis. To accomplish this understanding theoretical studies have to be done by decoupling the parameters given in 2.4. Furthermore there have to be done more studies to gain an understanding on the frequency dependency of quantities like the scaling of the jet diameter, the spectral index, the magnetic field and the brightness temperature itself. These accomplishments would increase our understanding of extra galactic jets and could lead to method to wholly understand the jet formation including the role of the super massive black hole as the central engine.

TABLE 4.1: Power law gradient indices  $s$  for all considered sources with  $\Delta\mathcal{X}^2$  and degree of freedom

source	$s$	$\Delta\mathcal{X}^2$	degree of freedom	$\sigma_{f_\nu}$ [%]	$\sigma_{a_{\max,\min}}$ [%]
1101 + 384	$-2.039 \pm 0.030$	2.98	109	10	20
1101 + 384	$-2.039 \pm 0.030$	2.23	109	20	20
1101 + 384	$-2.039 \pm 0.030$	1.4	109	10	30
1101 + 384	$-2.039 \pm 0.030$	1.2	109	20	30
0133 + 476	$-2.145 \pm 0.028$	16.75	121	10	20
0333 + 321	$-1.800 \pm 0.040$	10.58	114	10	20
0234 + 285	$-2.130 \pm 0.040$	10.32	79	10	20
0106 + 013	$-2.20 \pm 0.07$	7.73	40	10	20
0224 + 671	$-2.32 \pm 0.04$	23.60	71	10	20
0122 - 003	$-1.45 \pm 0.06$	11.82	27	10	20
1652 + 398	$-1.197 \pm 0.020$	6.70	109	10	20

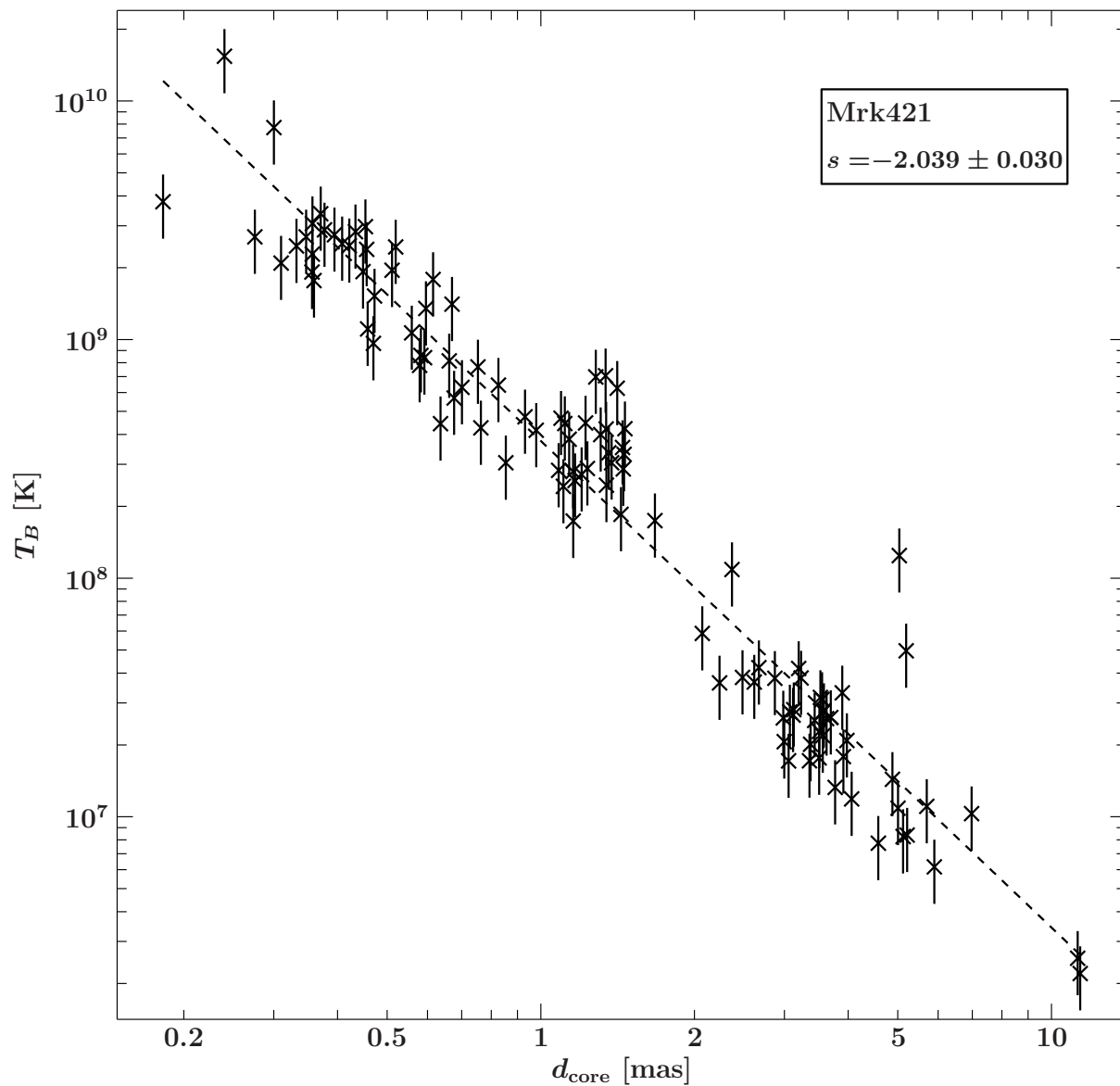


FIGURE 4.1: Gradient of the brightness temperature fitted with a pure power law for 1101+384 (Mrk 421); the power law index  $s = -2.039 \pm 0.030$   $\Delta\chi^2 = 2.98$ ; degrees of freedom: 109.

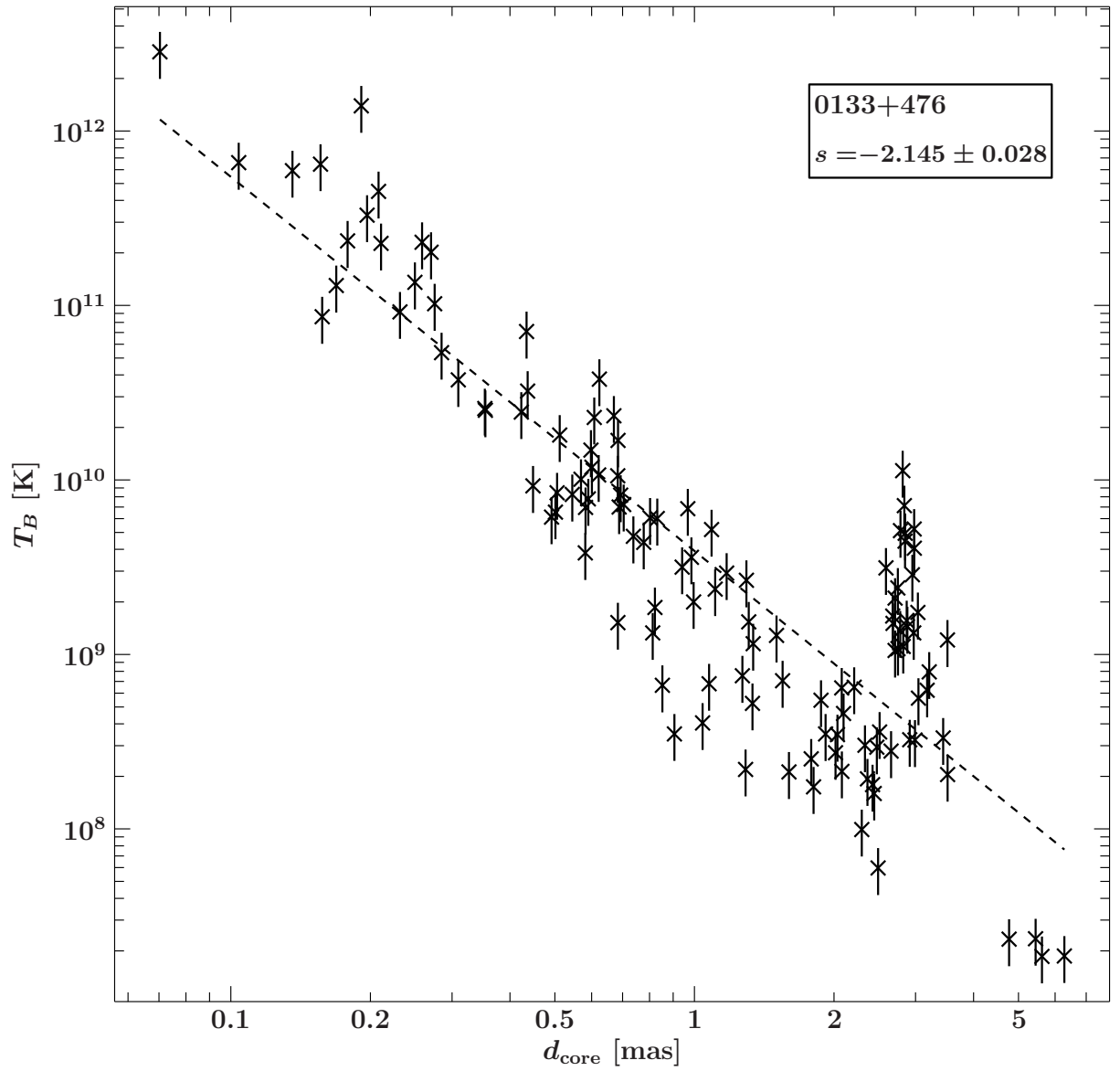


FIGURE 4.2: Gradient of the brightness temperature fitted with a pure power law for 0133+476; the power law index  $s = -2.145 \pm 0.028$ ;  $\Delta\chi^2 = 16.75$ ; degrees of freedom: 121.

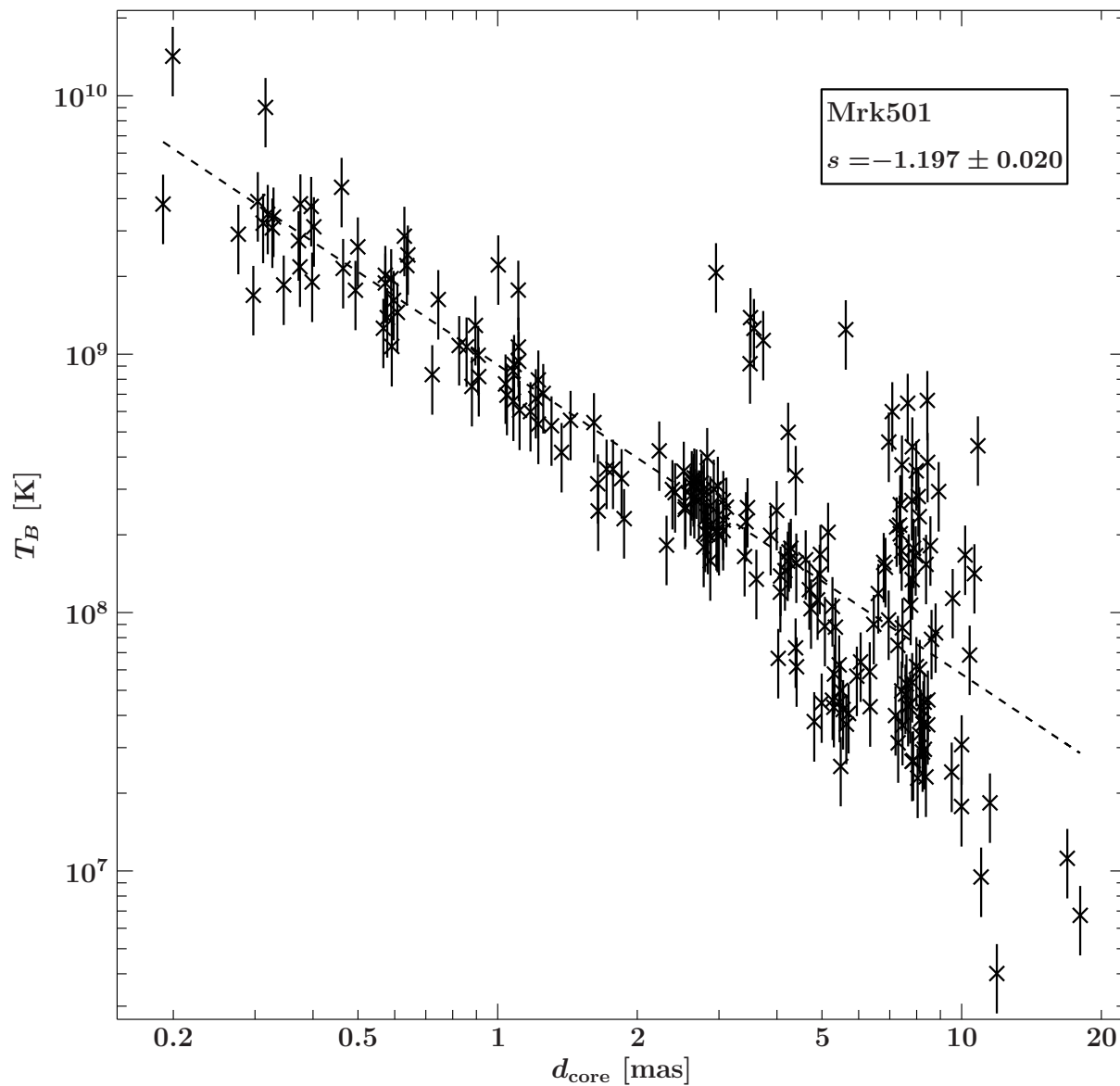


FIGURE 4.3: Gradient for the brightness temperature fitted with a pure power law for 1652+398 (Mrk501) ; the power law index  $s = -1.197 \pm 0.020$ .;  $\Delta\chi^2 = 6.70$ ; degrees of freedom: 218

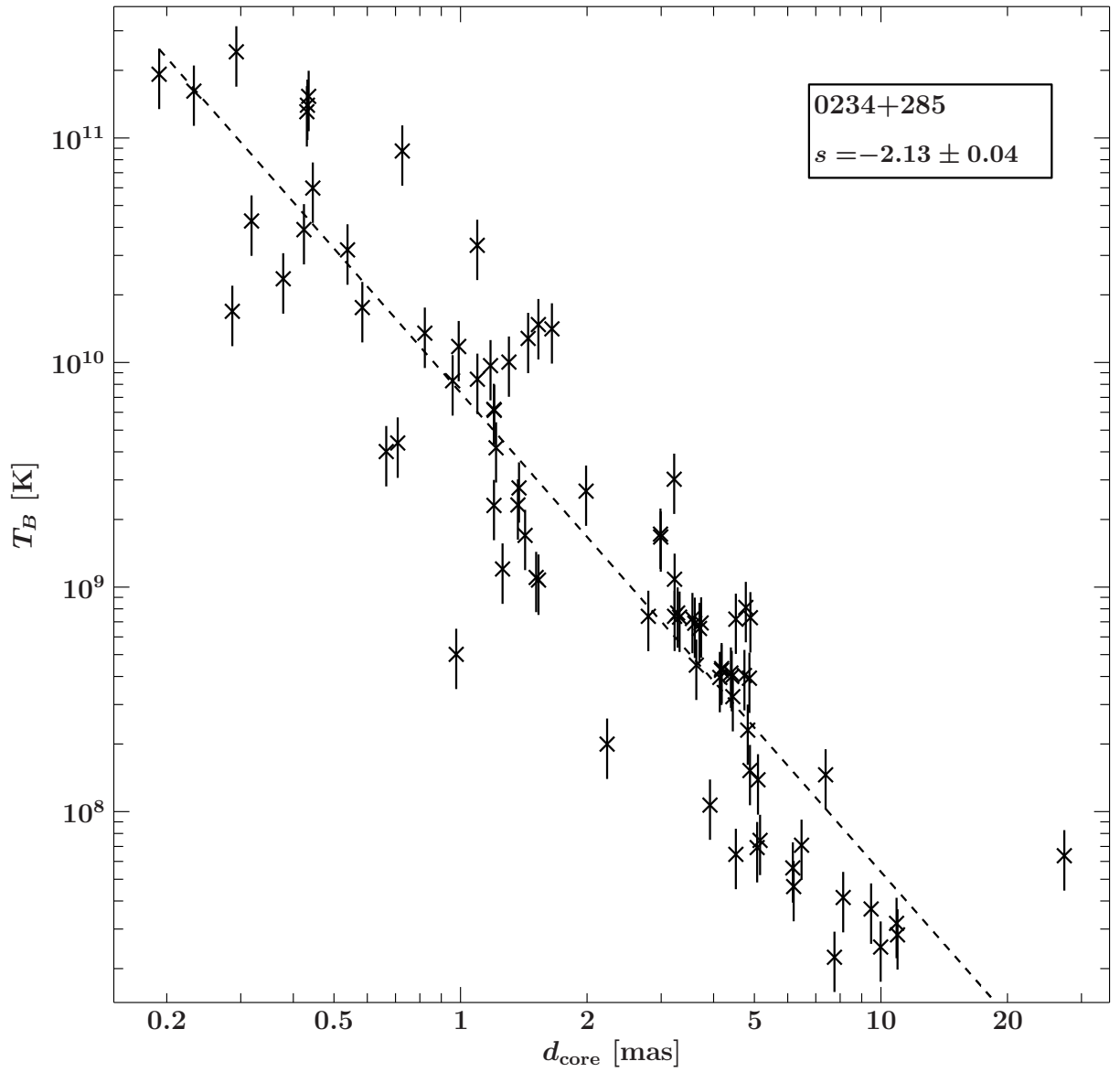


FIGURE 4.4: Gradient of the brightness temperature fitted with a pure power law for 0234+285; the power law index  $s = -2.13 \pm 0.04$   $\Delta\chi^2 = 10.32$ ; degrees of freedom: 79.

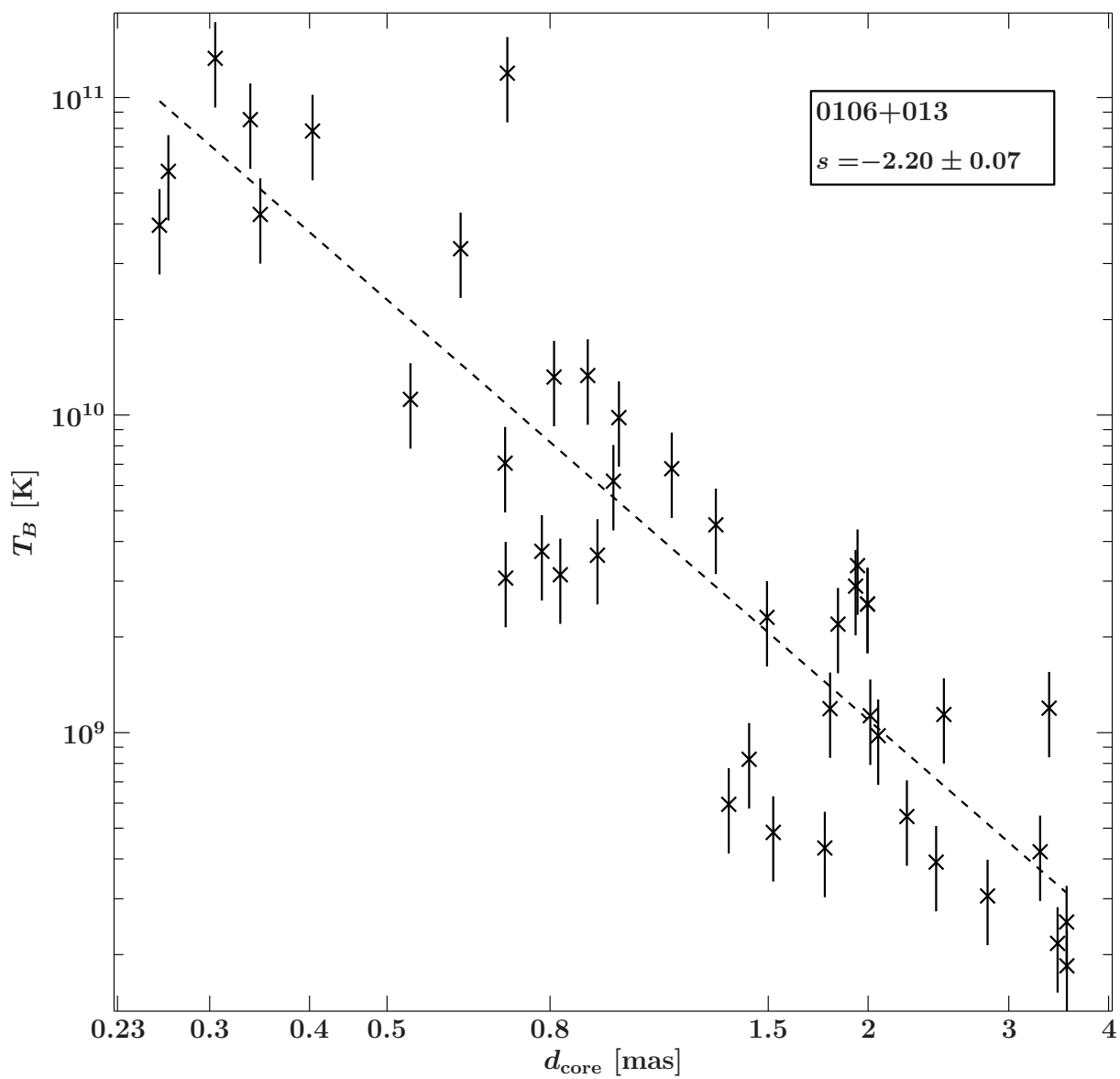


FIGURE 4.5: Gradient of the brightness temperature fitted with a pure power law for 0106+013; the power law index  $s = -2.20 \pm 0.07$ ;  $\Delta\chi^2 = 7.73$ ; degrees of freedom: 40.

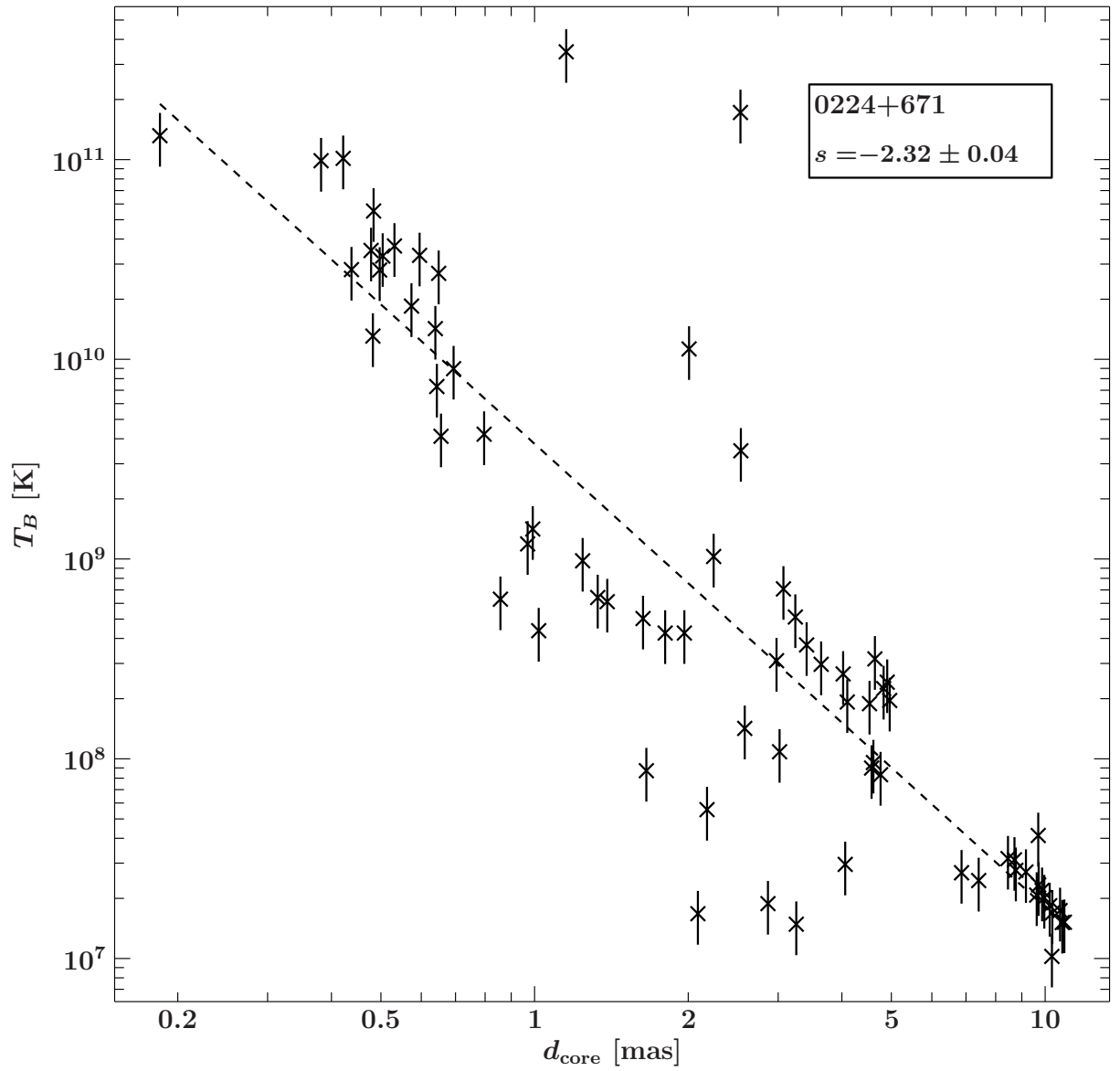


FIGURE 4.6: Gradient for the brightness temperature fitted with a pure power law for 0224+671; the power law index  $s = -2.32 \pm 0.04$ ;  $\Delta\chi^2 = 23.60$ ; degrees of freedom: 71.

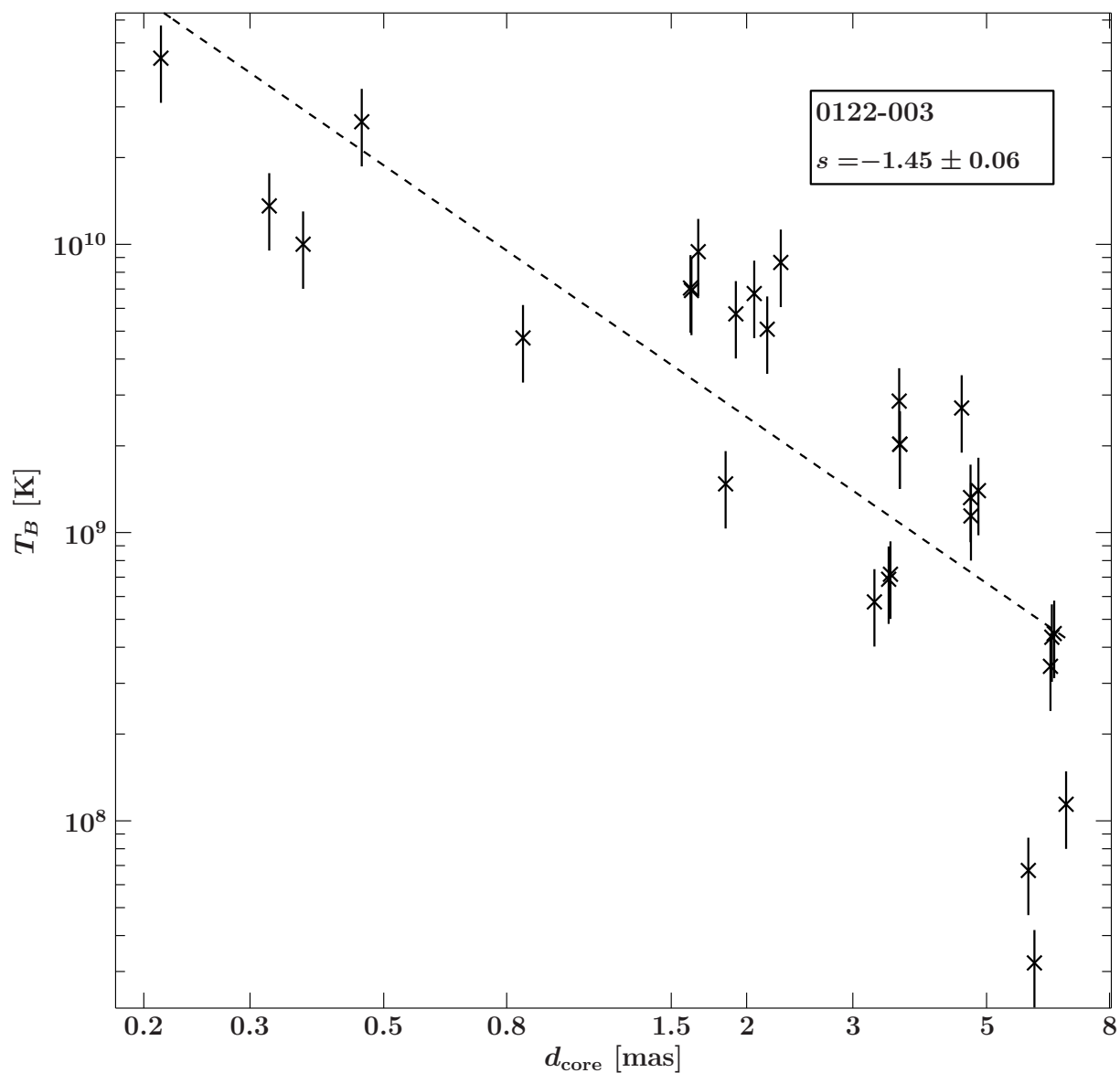


FIGURE 4.7: Gradient of the brightness temperature fitted with a pure power law for 0122-003; the power law index  $s = -2.20 \pm 0.07$ ;  $\Delta\chi^2 = 7.73$ ; degrees of freedom: 40.

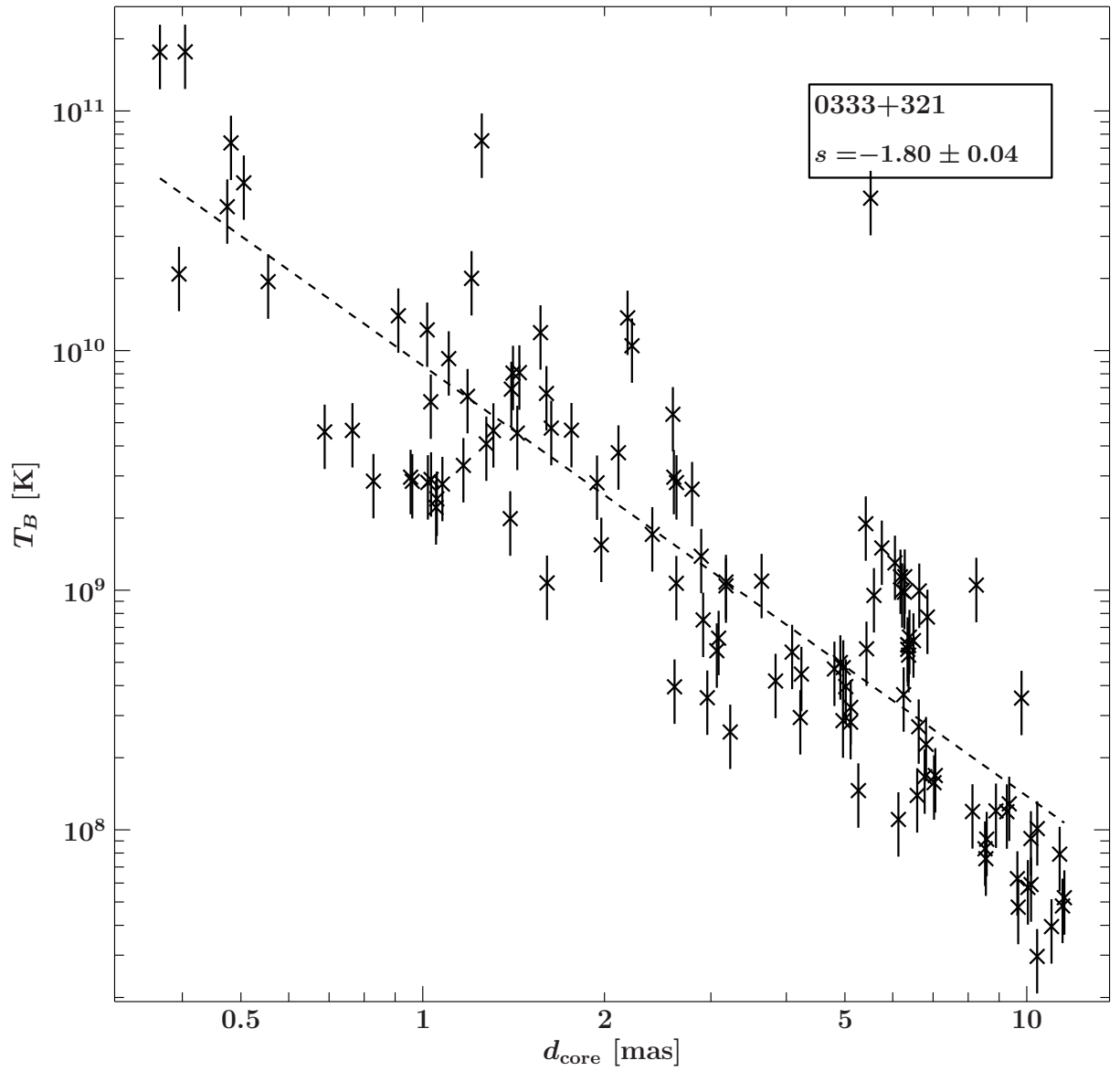


FIGURE 4.8: Gradient of the brightness temperature fitted with a pure power law for 0333+321; the power law index  $s = -1.80 \pm 0.04$ ;  $\Delta\chi^2 = 10.58$ ; degrees of freedom: 114.

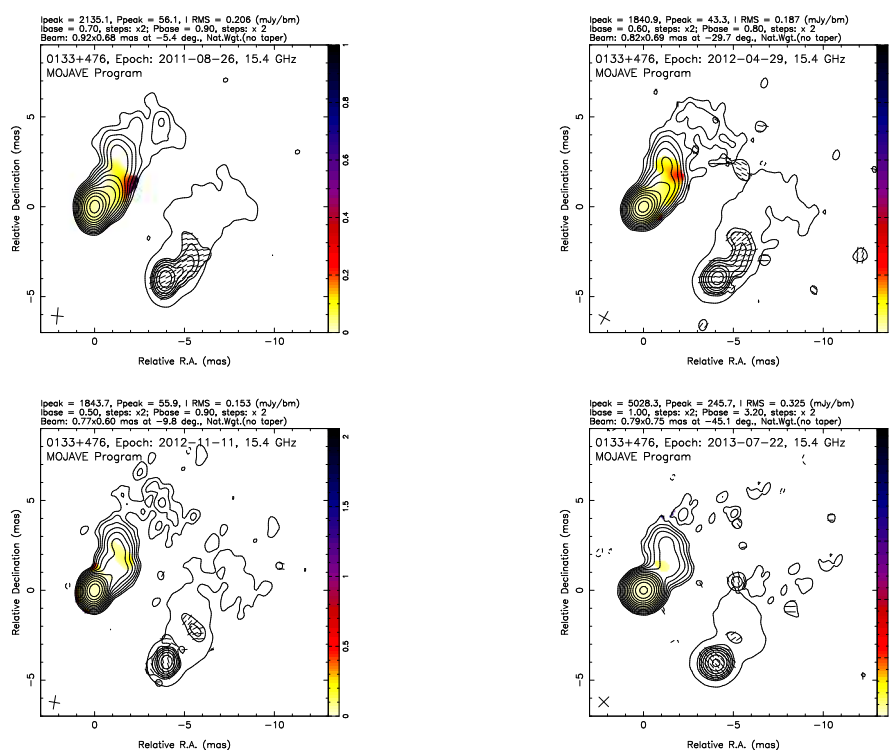


FIGURE 4.9: spectral index and polarisation map for 0133+476

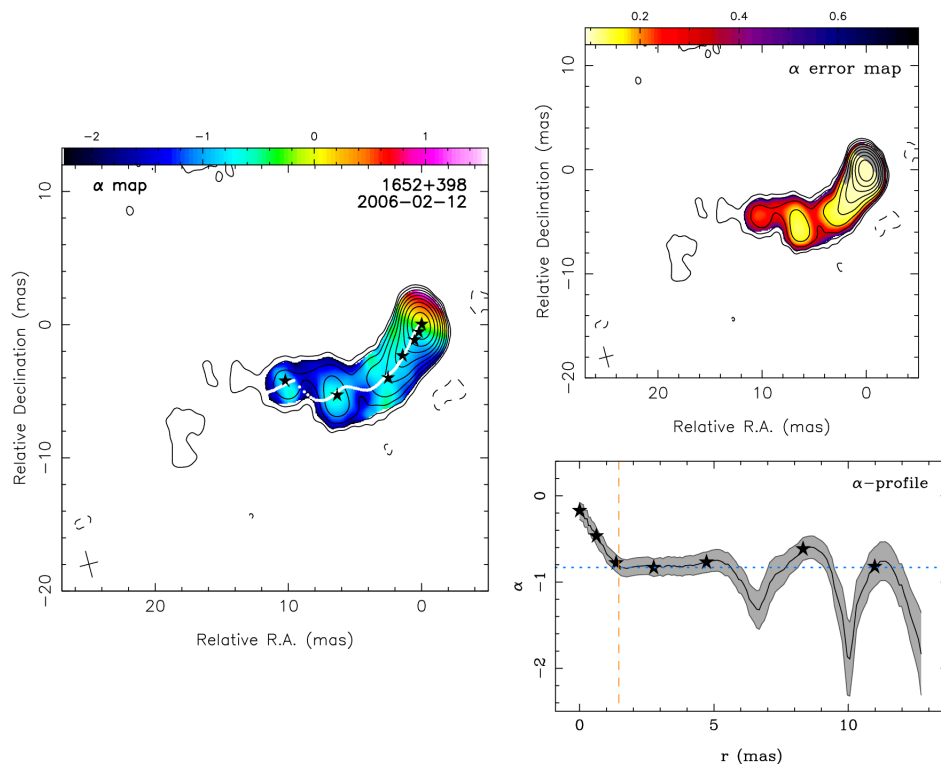


FIGURE 4.10: spectral index maps for 1652+398

TABLE 4.2: Power law gradient indices  $s$  for all considered sources with sub classification

source	Königl (1981)	Blandford & Königl (1979)	excess	power law
0133 + 476	yes	no	yes	yes
0333 + 321	yes	no	no	yes
0234 + 285	yes	no	no	yes
1101 + 384	yes	no	no	yes
0106 + 013	yes	no	no	yes
0224 + 671	yes	no	no	yes
0122 – 003	yes	no	no	yes
1652 + 398	yes	no	yes	yes

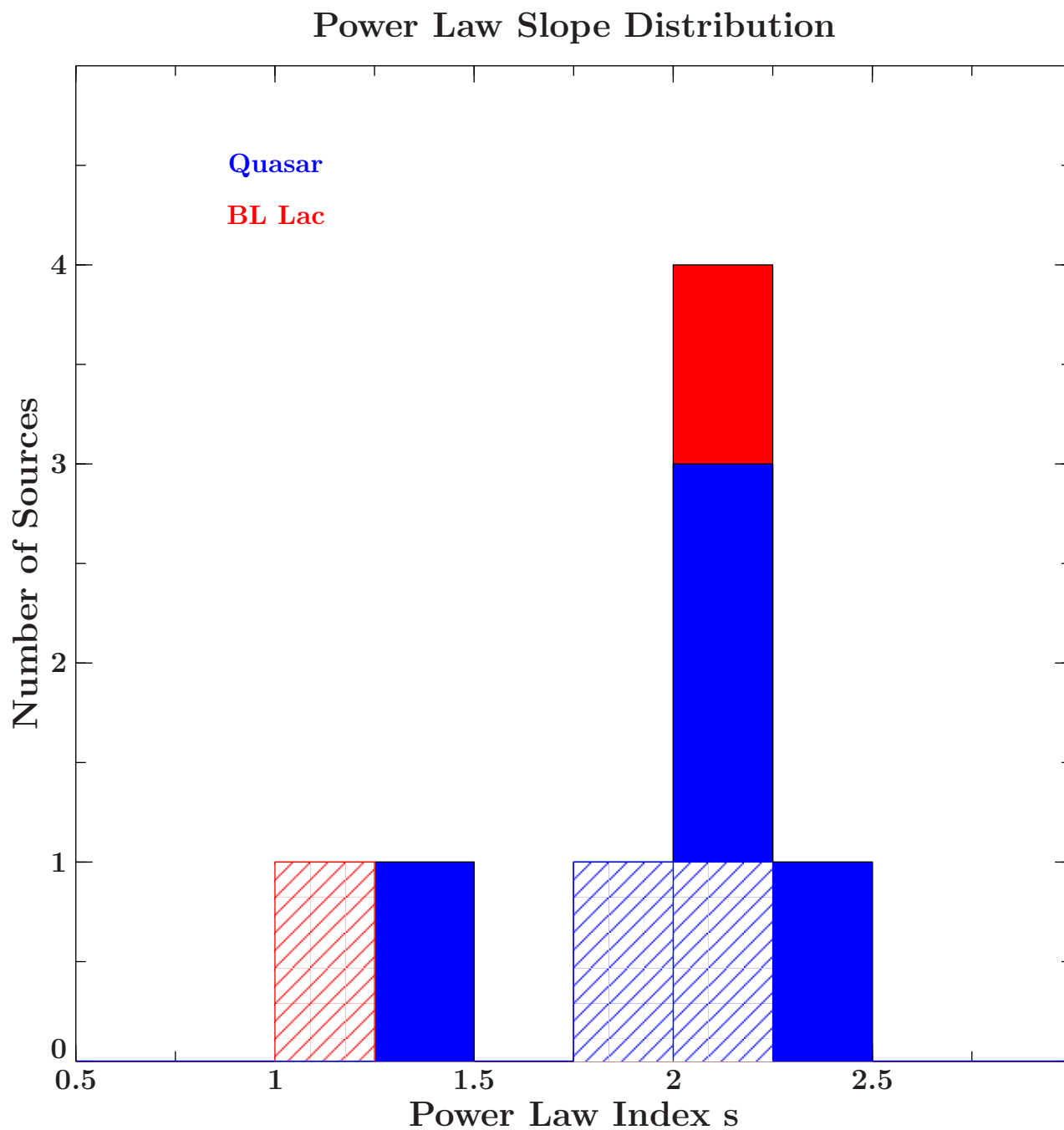


FIGURE 4.11: power law slope distribution of considered jets; the distribution of BL Lacs is marked red, the distribution for Quasars is marked blue. The hatched columns mark the sources for which a brightness temperature excess is assessed

# List of Figures

1.1	Visual summary of the unification model based on the summary of Urry & Padovani (1995); At the center is the SMBH surrounded by the accretion disc and the dust torus. On the left picture the radio loud AGN are illustrated, on the right picture the radio quiet AGN are illustrated. Credit: NASA/CXC/M.Weiss; edited by Jonas Trüstedt . . . . .	9
3.1	a) basic concept of a two element interferometer;b) illustrates the receiving element in the direction $\vec{s}$ and and solid angle $d^2\Omega$ for an extended source; c) introduction of the uv-plane in relation to the celestial sphere with the North Celestial Pole (NCP); $x$ and $y$ are the components of the offset $\sigma$ ; Credit: Burke & Graham-Smith (2009) . . . . .	20
3.2	The $(u, v)$ -plain coverage of the MERLIN interferometer array is illustrated while in use of six telescopes at a observation time of 8 hours at different declinations $\delta$ ; Credit: Burke & Graham-Smith (2009) . . . . .	21
3.3	For each of my chosen sources a stacked image is given in this figure which means that all imaged epochs are stacked together to obtain an overview of the sources components during the whole observation time span taken from the MOJAVE data base; Lister et al. (2009). . . . .	25
3.4	1652+398 (Mrk501); epoch 2009-01-07; description will follow from the left top corner to the right bottom corner;a)residual map without component; b) clean map with first component; c) clean map with two components; d) clean map with spherical jet model; e) clean map with elliptical jet model . . . . .	27
4.1	Gradient of the brightness temperature fitted with a pure power law for 1101+384 (Mrk 421); the power law index $s = -2.039 \pm 0.030$ $\Delta\chi^2 = 2.98$ ; degrees of freedom: 109. . . . .	34
4.2	Gradient of the brightness temperature fitted with a pure power law for 0133+476; the power law index $s = -2.145 \pm 0.028$ ; $\Delta\chi^2 = 16.75$ ; degrees of freedom: 121. . . . .	35
4.3	Gradient for the brightness temperature fitted with a pure power law for 1652+398 (Mrk501) ; the power law index $s = -1.197 \pm 0.020$ .; $\Delta\chi^2 = 6.70$ ; degrees of freedom: 218 . . . . .	36
4.4	Gradient of the brightness temperature fitted with a pure power law for 0234+285; the power law index $s = -2.13 \pm 0.04$ $\Delta\chi^2 = 10.32$ ; degrees of freedom: 79. . . . .	37
4.5	Gradient of the brightness temperature fitted with a pure power law for 0106+013; the power law index $s = -2.20 \pm 0.07$ ; $\Delta\chi^2 = 7.73$ ; degrees of freedom: 40. . . . .	38

---

4.6	Gradient for the brightness temperature fitted with a pure power law for 0224+671; the power law index $s = -2.32 \pm 0.04$ ; $\Delta\chi^2 = 23.60$ ; degrees of freedom: 71. . . . .	39
4.7	Gradient of the brightness temperature fitted with a pure power law for 0122-003; the power law index $s = -2.20 \pm 0.07$ ; $\Delta\chi^2 = 7.73$ ; degrees of freedom: 40. . . . .	40
4.8	Gradient of the brightness temperature fitted with a pure power law for 0333+321; the power law index $s = -1.80 \pm 0.04$ ; $\Delta\chi^2 = 10.58$ ; degrees of freedom: 114. . . . .	41
4.10	spectral index maps for 1652+398 . . . . .	42
4.11	power law slope distribution of considered jets; the distribution of BL Lacs is marked red, the distribution for Quasars is marked blue. The hatched columns mark the sources for which a brightness temperature excess is assessed . . . . .	44

# List of Tables

1.1	Summary of the Unification Model Credit: Matthias Kadler, edited by Paul Ray Burd . . . . .	10
2.1	Canonical Values for the power indices from equation 2.15 based on the assumptions given at the beginning of chapter 2 with the restrictions of Blandford & Königl (1979) and Königl (1981) . . . . .	16
3.1	Selected Sources with B1950 and common name, AGN classification and redshift . . . . .	23
3.2	Spherical Gaussian Components contained in the clean plot of 1652+398 (MRK501) from the epoch 2009-01-07 which is seen in Fig3.4 d); The values for the considered quantities in this table are taken from the DIFMAP log which is created when fitting models into the visibility data . . . . .	26
3.3	Elliptical Gaussian Components contained in the clean of 1652+398 (MRK501) from the epoch 2009-01-07 which is seen in Fig3.4 e); The values for the considered quantities in this table are taken from the DIFMAP log which is created when fitting models into the visibility data. . . . .	26
4.1	Power law gradient indices $s$ for all considered sources with $\Delta\chi^2$ and degree of freedom . . . . .	33
4.2	Power law gradient indices $s$ for all considered sources with sub classification	43
A.1	0133+476; Each epoch with the corresponding component is listed; the date is given as yyyy-mm-dd; the brightness temperature and the core distance for each component is listed. . . . .	55
A.2	0234+285; Each epoch with the corresponding component is listed; the date is given as yyyy-mm-dd; the brightness temperature and the core distance for each component is listed. . . . .	60
A.3	1101+384; Each epoch with the corresponding component is listed; the date is given as yyyy-mm-dd; the brightness temperature and the core distance for each component is listed. . . . .	63
A.4	0106+013; Each epoch with the corresponding component is listed; the date is given as yyyy-mm-dd; the brightness temperature and the core distance for each component is listed. . . . .	67
A.5	0122-003; Each epoch with the corresponding component is listed; the date is given as yyyy-mm-dd; the brightness temperature and the core distance for each component is listed. . . . .	69
A.6	1652+398; Each epoch with the corresponding component is listed; the date is given as yyyy-mm-dd; the brightness temperature and the core distance for each component is listed. . . . .	70

---

A.7	0333+321; Each epoch with the corresponding component is listed; the date is given as yyyy-mm-dd; the brightness temperature and the core distance for each component is listed. . . . .	76
A.8	0224+671; Each epoch with the corresponding component is listed; the date is given as yyyy-mm-dd; the brightness temperature and the core distance for each component is listed. . . . .	80

# Bibliography

Albert J., Aliu E., Anderhub H., et al., 2007, *apj* 669, 862

Antonucci R., 1993, *araa* 31, 473

Antonucci R., Barvainis R., 1990, *apjl* 363, L17

Bass M., Stryland E.W.V., Williams D.R., Wolfe W.L., 1995, *Handbook of Optics*  
Volume II Devices, Measurements, and Properties 2nd edition, NY: McGraw-Hill,  
INC

Blandford R.D., Königl A., 1979, *ApJ* 232, 34

Blumenthal G.R., Gould R.J., 1970, *Reviews of Modern Physics* 42, 237

Boisse P., Bergeron J., 1988, *aap* 192, 1

Bregman J.N., 1990, *aapr* 2, 125

Bridle A.H., Perley R.A., 1984, *araa* 22, 319

Burbidge E.M., 1970, *apjl* 160, L33

Burke B.F., Graham-Smith F., 2009, *An Introduction to Radio Astronomy*, Cambridge  
University Press

Camenzind M., 2007, *Compact objects in astrophysics : white dwarfs, neutron stars,  
and black holes*, Berlin: Springer-Verlag

Cohen R.D., Smith H.E., Junkkarinen V.T., Burbidge E.M., 1987, *apj* 318, 577

Hewett P.C., Foltz C.B., Chaffee F.H., 1995, *aj* 109, 1498

Holt S.S., Neff S.G., Urry C.M., (eds.) 1992, *Testing the AGN paradigm; Proceed-  
ings of the 2nd Annual Topical Astrophysics Conference*, Univ. of Maryland, College  
Park, Oct. 14-16, 1991, Vol. 254 of *American Institute of Physics Conference Series*,  
American Institute of Physics Conference Series

Hook I.M., McMahon R.G., Irwin M.J., Hazard C., 1996, *mnras* 282, 1274

- Jones D.H., Read M.A., Saunders W., et al., 2009, *mnras* 399, 683
- Kadler M., Ros E., Lobanov A.P., et al., 2004, *A&A* 426, 481
- Kellermann K.I., Pauliny-Toth I.I.K., Williams P.J.S., 1969, *apj* 157, 1
- Kovalev Y.Y., Kellermann K.I., Lister M.L., et al., 2005, *aj* 130, 2473
- Königl A., 1981, *ApJ* 243, 700
- Lawrence C.R., Pearson T.J., Readhead A.C.S., Unwin S.C., 1986, *aj* 91, 494
- Lister M.L., Cohen M.H., Homan D.C., et al., 2009, *aj* 138, 1874
- Mannheim K., 1993, *aap* 269, 67
- Marziani P., Sulentic J.W., Zamanov R., et al., 2003, *apjs* 145, 199
- Misner C.W., Thorne K.S., Wheeler J.A., 1973, *Gravitation*
- Osmer P.S., Porter A.C., Green R.F., 1994, *apj* 436, 678
- Perlman E.S., Padovani P., Giommi P., et al., 1998, *aj* 115, 1253
- Peterson B.M., Ferrarese L., Gilbert K.M., et al., 2004, *apj* 613, 682
- Readhead A.C.S., 1994, *apj* 426, 51
- Rees M.J., 1967, *mnras* 137, 429
- Robson I., 1996, *Active galactic nuclei*, Wiley, Chichester: Praxis Publishing
- Rybicki G.B., Lightman A.P., 1979, *Radiative processes in astrophysics*, New York, Wiley-Interscience, 1979. 393 p.
- Schneider D.P., Richards G.T., Fan X., et al., 2002, *aj* 123, 567
- Shakura N.I., Sunyaev R.A., 1973, *aap* 24, 337
- Shaw M.S., Romani R.W., Cotter G., et al., 2012, *apj* 748, 49
- Shepherd M.C., 1997, In: Hunt G., Payne H. (eds.) *Astronomical Data Analysis Software and Systems VI*, Vol. 125. *Astronomical Society of the Pacific Conference Series*, p. 77
- Sowards-Emmerd D., Romani R.W., Michelson P.F., et al., 2005, *apj* 626, 95
- Steidel C.C., Sargent W.L.W., 1991, *apj* 382, 433
- Stickel M., Fried J.W., Kuehr H., 1993, *aaps* 98, 393
- Stickel M., Meisenheimer K., Kuehr H., 1994, *aaps* 105, 211

Stoche J.T., Morris S.L., Weymann R.J., Foltz C.B., 1992, *apj* 396, 487

Thompson A.R., Moran J.M., Swenson G.W., 1986, *Interferometry and synthesis in radio astronomy*, New York, Wiley-Interscience, 1986, 554 p.

Ulrich M.H., Kinman T.D., Lynds C.R., et al., 1975, *apj* 198, 261

Ulrich M.H., Maraschi L., Urry C.M., 1997, *araa* 35, 445

Urry C.M., Padovani P., 1995, *pasp* 107, 803

Vestergaard M., Peterson B.M., 2006, *apj* 641, 689

Wills D., Lynds R., 1978, *apjs* 36, 317

Wright A.E., Ables J.G., Allen D.A., 1983, *mnras* 205, 793

## *Acknowledgements*

I want to express my deep gratitude towards those who made it possible for me to work on this project and write a thesis about it.

Firstly I thank Matthias Kadler for granting me the privilege to become a part of his group and providing this project on which I were able to work for my thesis. My interest for the work of his group arouse when he held a talk at "Physik am Samstag" about multi wavelength observations and extragalactic jets. I am deeply thankful for the chance I was given by Matthias Kadler to do my first steps into scientific research on extragalactic jets and supervising this thesis.

Another person without whom this work would not have been viable in this form, is Till Steinbring. He introduced me to this project and taught me the basics I needed to know to accomplish this thesis. He always took some of his time to look over the work I did and discuss the things I needed to work over again. Till taught me many aspect of scientific work and thesis writing. I am deeply thankful to have a mentor like him.

Whenever I had problems with any kind of software I used for this work, Jonas Trüstedt could help me to find solutions. He also explained me how to work with radio data to obtain images and model fits. Thus he contributed a very important aspect for this thesis to become manifest.

Also for the of Annika Kreikenbohm and Robert Schulz I am deeply thankful. They helped me to solve statistical problems with the power law fits in my plots and also wrote new ISIS scripts for me to overwork my plots.

I want to thank all the members of the chair of astronomy, especially the members of Matthias Kadler's group, who integrated me without hesitation and always were open for discussions which contributed to my understanding of the matter.

At last I deeply want to thank my mother Evelyn, my two sisters, Natalie and Thea, and my love Svenja. Due to their support and strong backing I was able to do my studies in Physics and Astronomy until this day.

This research has made use of data from the MOJAVE database that is maintained by the MOJAVE team [Lister et al. \(2009\)](#)

*Mitakuye Oyasin*

# Declaration of Authorship

I, Paul Ray Burd, declare that this thesis titled, 'Measuring Brightness Temperature Gradients in Extragalactic Jets' and the work presented in it are my own. I confirm that:

- This work was done wholly or mainly while in candidature for a research degree at this University.
- Where any part of this thesis has previously been submitted for a degree or any other qualification at this University or any other institution, this has been clearly stated.
- Where I have consulted the published work of others, this is always clearly attributed.
- Where I have quoted from the work of others, the source is always given. With the exception of such quotations, this thesis is entirely my own work.
- I have acknowledged all main sources of help.
- Where the thesis is based on work done by myself jointly with others, I have made clear exactly what was done by others and what I have contributed myself.

Signed:

---

Date:

---



# Appendix A

## Appendix

TABLE A.1: 0133+476; Each epoch with the corresponding component is listed; the date is given as yyyy-mm-dd; the brightness temperature and the core distance for each component is listed.

Epoch	Component	Date	Brightness Temperature (K)	Core Distance (mas)
0	4	1996-07-10	1.26E+012	0.00E+000
0	3		2.02E+011	2.70E-001
0	2		3.50E+008	9.05E-001
0	1		1.51E+009	2.68E+000
1	4	1997-28-08	9.46E+012	0.00E+000
1	3		2.27E+011	2.11E-001
1	2		2.28E+010	6.08E-001
1	1		6.79E+008	1.08E+000
2	4	1994-08-31	1.65E+012	0.00E+000
2	3		8.18E+009	6.93E-001
2	2		1.66E+009	2.68E+000
2	1		4.59E+008	2.10E+000
3	3	1995-01-20	4.07E+012	0.00E+000
3	2		6.65E+008	8.53E-001
3	1		2.10E+009	2.71E+000
4	4	1996-08-28	1.38E+013	0.00E+000
4	3		3.29E+011	1.97E-001
4	2		2.12E+008	1.60E+000
4	1		1.37E+009	2.78E+000
5	5	1997-07-13	4.06E+012	0.00E+000
5	4		1.02E+011	2.75E-001
5	3		1.69E+010	6.84E-001
5	2		1.11E+009	2.82E+000
5	1		9.91E+007	2.30E+000

Epoch	Component	Date	Brightness Temperature (K)	Core Distance (mas)
6	4	1999-01-02	1.36E+013	1.98E-001
6	3		3.15E+010	0.00E+000
6	2		9.25E+009	4.49E-001
6	1		1.94E+008	2.36E+000
7	3	1999-07-24	5.58E+012	0.00E+000
7	2		7.23E+009	7.04E-001
7	1		1.60E+008	2.44E+000
8	3	1999-08-04	3.39E+012	0.00E+000
8	2		6.99E+009	6.88E-001
8	1		5.97E+007	2.49E+000
9	4	1999-10-16	5.36E+012	0.00E+000
9	3		2.57E+010	3.53E-001
9	2		2.37E+009	1.11E+000
9	1		1.21E+009	3.51E+000
10	5	1999-12-23	5.43E+012	0.00E+000
10	4		7.09E+010	4.34E-001
10	3		3.60E+009	9.85E-001
10	2		3.32E+008	3.44E+000
10	1		5.47E+008	1.88E+000
11	2	2000-01-11	3.32E+012	0.00E+000
11	1		3.16E+009	9.41E-001
12	3	2000-06-27	5.83E+012	0.00E+000
12	2		6.12E+009	4.92E-001
12	1		1.74E+008	1.81E+000
13	4	2000-07-28	2.16E+014	0.00E+000
13	3		5.93E+011	1.36E-001
13	2		4.75E+009	7.39E-001
13	1		7.06E+008	1.55E+000
14	3	2000-09-27	5.03E+015	0.00E+000
14	2		2.30E+011	2.59E-001
14	1		2.00E+009	9.96E-001
15	3	2001-06-30	2.62E+013	0.00E+000
15	2		5.37E+010	2.85E-001
15	1	2001-08-25	2.93E+009	1.17E+000
16	4		1.68E+013	2.65E-001
16	3		9.30E+010	0.00E+000
16	2		6.96E+009	5.82E-001
16	1		2.52E+008	1.79E+000
17	3	2001-11-02	7.45E+012	0.00E+000
17	2		8.25E+009	5.45E-001
17	1		2.73E+008	2.02E+000

Epoch	Component	Date	Brightness Temperature (K)	Core Distance (mas)
18	3	2002-01-07	9.51E+012	0.00E+000
18	2		8.44E+009	5.06E-001
18	1		3.50E+008	1.92E+000
19	3	2002-02-02	1.53E+013	0.00E+000
19	2		6.01E+009	8.32E-001
19	1		1.13E+010	2.81E+000
20	3	2002-06-15	8.00E+012	0.00E+000
20	2		7.80E+009	5.91E-001
20	1		3.47E+008	2.03E+000
21	7	2003-03-05	1.13E+013	0.00E+000
21	6		1.30E+011	1.69E-001
21	5		6.06E+009	8.02E-001
21	4		1.54E+009	1.31E+000
21	3		5.24E+008	1.33E+000
21	2		1.79E+008	2.42E+000
21	1		1.44E+009	2.88E+000
22	5	2004-06-11	1.03E+015	0.00E+000
22	4		6.58E+011	1.04E-001
22	3		3.23E+010	4.37E-001
22	2		7.54E+008	1.27E+000
22	1		2.40E+009	2.75E+000
23	7	2005-03-05	5.38E+012	0.00E+000
23	6		8.61E+010	1.57E-001
23	5		1.01E+010	5.69E-001
23	4		1.15E+009	1.34E+000
23	3		4.94E+009	2.85E+000
23	2		2.14E+008	2.08E+000
23	1		3.13E+009	2.59E+000
24	6	2005-09-16	2.61E+012	0.00E+000
24	5		3.74E+010	3.09E-001
24	4		1.52E+009	6.84E-001
24	3		5.12E+009	2.78E+000
24	2		3.02E+008	2.33E+000
24	1		1.87E+007	6.28E+000
25	5	2006-08-09	2.32E+012	0.00E+000
25	4		1.81E+010	5.12E-001
25	3		4.05E+008	1.04E+000
25	2		7.12E+009	2.84E+000
25	1		4.46E+009	2.85E+000
26	4	2004-04-18	5.76E+012	0.00E+000
26	3		1.33E+009	8.13E-001
26	2		5.23E+009	2.98E+000
26	1		1.08E+009	2.75E+000

Epoch	Component	Date	Brightness Temperature (K)	Core Distance (mas)
27	5	2008-06-25	3.67E+012	0.00E+000
27	4		2.35E+011	1.79E-001
27	3		3.82E+009	5.81E-001
27	2		4.06E+009	2.98E+000
27	1		3.24E+008	2.91E+000
28	8	2009-06-25	5.90E+012	1.57E-001
28	7		1.67E+012	0.00E+000
28	6		9.19E+010	2.32E-001
28	5		1.48E+010	5.98E-001
28	4		1.86E+009	8.22E-001
28	3		2.86E+009	2.95E+000
28	2		6.23E+008	3.18E+000
28	1		2.94E+008	2.47E+000
29	6	2009-12-10	4.20E+012	1.53E-001
29	5		1.53E+012	0.00E+000
29	4		3.78E+010	6.24E-001
29	3		1.36E+011	2.50E-001
29	2		1.18E+010	6.01E-001
29	1		1.74E+009	3.03E+000
30	5	2010-08-06	2.17E+012	2.30E-001
30	4		1.63E+011	0.00E+000
30	3		1.07E+010	6.21E-001
30	2		1.33E+009	2.97E+000
30	1		3.23E+008	2.99E+000
31	6	2010-11-20	6.40E+012	0.00E+000
31	5		1.39E+012	1.91E-001
31	4		2.33E+010	6.70E-001
31	3		6.84E+009	9.68E-001
31	2		8.55E+008	3.20E+000
31	1		2.79E+008	2.66E+000
32	7	2011-02-27	9.71E+012	0.00E+000
32	6		4.50E+011	2.08E-001
32	5		1.06E+010	6.83E-001
32	4		5.19E+009	1.09E+000
32	3		7.94E+008	3.21E+000
32	2		3.59E+008	2.51E+000
32	1		2.33E+007	4.77E+000
33	8	2011-08-26	7.84E+013	0.00E+000
33	7		2.84E+012	7.03E-002
33	6		2.45E+010	4.23E-001
33	5		2.19E+008	1.29E+000
33	4		2.66E+009	1.29E+000
33	3		4.95E+011	1.33E+000
33	2		5.61E+008	3.04E+000
33	1		1.86E+007	5.62E+000

---

Epoch	Component	Date	Brightness Temperature (K)	Core Distance (mas)
34	8	2012-04-29	9.70E+012	0.00E+000
34	7		6.46E+011	1.56E-001
34	6		4.39E+009	7.77E-001
34	5		1.28E+009	1.50E+000
34	4		1.56E+009	2.87E+000
34	3		2.05E+008	3.52E+000
34	2		1.05E+009	2.71E+000
34	1		2.35E+007	5.44E+000
35	3	2012-11-11	5.27E+012	0.00E+000
35	2		6.54E+009	5.01E-001
35	1		6.43E+008	2.08E+000
36	3	2013-07-22	4.04E+012	0.00E+000
36	2		2.51E+010	3.54E-001
36	1		6.49E+008	2.21E+000

---

TABLE A.2: 0234+285; Each epoch with the corresponding component is listed; the date is given as yyyy-mm-dd; the brightness temperature and the core distance for each component is listed.

Epoch	Component	Date	Brightness Temperature (K)	Core Distance (mas)
0	4	1995-01-27	5.69E+012	0.00E+000
0	3		6.19E+009	1.20E+000
0	2		4.26E+008	4.18E+000
0	1		1.72E+009	2.99E+000
1	4	1995-04-07	5.67E+012	0.00E+000
1	3		6.13E+009	1.20E+000
1	2		4.14E+008	4.40E+000
1	1		1.67E+009	2.99E+000
2	4	1995-12-15	6.42E+011	0.00E+000
2	3		4.38E+009	7.09E-001
2	2		4.00E+008	4.41E+000
2	1		7.41E+008	2.80E+000
3	3	1998-03-19	2.62E+011	0.00E+000
3	2		2.36E+010	3.78E-001
3	1		6.92E+008	3.74E+000
4	3	1996-01-13	7.99E+011	0.00E+000
4	2		4.01E+009	6.65E-001
4	1		7.35E+008	3.32E+000
5	6	1996-05-16	6.36E+007	2.73E+001
5	5		1.14E+012	0.00E+000
5	4		7.30E+008	4.89E+000
5	3		4.17E+009	1.21E+000
5	2		3.02E+009	3.22E+000
5	1		7.41E+008	3.23E+000
6	6	1997-08-10	2.13E+012	0.00E+000
6	5		1.69E+010	2.87E-001
6	4		1.07E+009	1.53E+000
6	3		1.08E+009	3.23E+000
6	2		3.93E+008	4.87E+000
6	1		1.46E+008	7.39E+000
7	5	1998-01-02	3.56E+012	0.00E+000
7	4		1.62E+011	2.32E-001
7	3		1.20E+009	1.26E+000
7	2		7.67E+008	3.28E+000
7	1		3.25E+008	4.44E+000
8	3	1998-04-27	2.24E+012	0.00E+000
8	2		4.27E+010	3.18E-001
8	1		6.91E+008	3.61E+000
9	2	1999-01-07	1.65E+012	0.00E+000
9	1		4.49E+008	3.64E+000

Epoch	Component	Date	Brightness Temperature (K)	Core Distance (mas)
10	4	1999-05-21	1.68E+012	0.00E+000
10	3		3.91E+010	4.24E-001
10	2		7.25E+008	3.56E+000
10	1		3.96E+008	4.14E+000
11	4	1999-07-17	2.29E+012	0.00E+000
11	3		3.17E+010	5.39E-001
11	2		6.54E+008	3.70E+000
11	1		2.31E+008	4.82E+000
12	2	2000-12-28	1.50E+012	0.00E+000
12	1		4.34E+008	4.18E+000
13	2	2002-11-23	7.41E+011	0.00E+000
13	1		1.52E+008	4.88E+000
14	3	2004-02-11	6.17E+011	0.00E+000
14	2		1.40E+011	4.32E-001
14	1		1.39E+008	5.10E+000
15	4	2005-03-23	1.50E+012	0.00E+000
15	3		1.53E+011	4.35E-001
15	2		8.11E+008	4.77E+000
15	1		5.62E+007	6.17E+000
16	4	2005-10-29	1.39E+012	0.00E+000
16	3		1.31E+011	4.31E-001
16	2		4.04E+008	4.73E+000
16	1		7.09E+007	6.47E+000
17	4	2006-09-06	6.72E+011	4.96E-001
17	3		1.10E+011	0.00E+000
17	2		1.76E+010	5.84E-001
17	1		7.45E+007	5.16E+000
18	4	2007-06-03	9.68E+011	0.00E+000
18	3		8.75E+010	7.27E-001
18	2		9.68E+009	1.18E+000
18	1		4.64E+007	6.20E+000
19	5	2008-07-30	1.35E+010	8.22E-001
19	4		1.09E+012	0.00E+000
19	3		7.20E+008	4.52E+000
19	2		3.33E+010	1.10E+000
19	1		4.14E+007	8.13E+000
20	3	2009-06-25	1.07E+008	3.92E+000
20	2		4.53E+011	0.00E+000
20	1		1.18E+010	9.90E-001
21	7	2010-09-17	3.54E+014	0.00E+000
21	6		7.30E+011	1.76E-001
21	5		5.02E+008	9.76E-001
21	4		2.68E+009	1.99E+000
21	3		8.42E+009	1.10E+000
21	2		8.29E+009	9.57E-001
21	1		3.68E+007	9.48E+000

Epoch	Component	Date	Brightness Temperature (K)	Core Distance (mas)
22	6	2011-05-26	7.00E+012	0.00E+000
22	5		2.31E+009	1.20E+000
22	4		2.00E+008	2.23E+000
22	3		2.42E+011	2.93E-001
22	2		1.28E+010	1.45E+000
22	1		2.50E+007	9.99E+000
23	4	2011-06-24	2.32E+009	1.37E+000
23	3		1.86E+012	0.00E+000
23	2		1.01E+010	1.30E+000
23	1		2.25E+007	7.75E+000
24	6	2011-09-12	2.26E+012	0.00E+000
24	5		5.98E+010	4.45E-001
24	4		6.45E+007	4.52E+000
24	3		2.76E+009	1.38E+000
24	2		1.47E+010	1.53E+000
24	1		2.83E+007	1.10E+001
25	7	2012-02-02	1.70E+009	1.42E+000
25	6		1.10E+009	1.51E+000
25	5		1.40E+014	0.00E+000
25	4		1.92E+011	1.92E-001
25	3		6.91E+007	5.07E+000
25	2		1.41E+010	1.65E+000
25	1		3.18E+007	1.09E+001

TABLE A.3: 1101+384; Each epoch with the corresponding component is listed; the date is given as yyyy-mm-dd; the brightness temperature and the core distance for each component is listed.

Epoch	Component	Date	Brightness Temperature (K)	Core Distance (mas)
0	4	1995-04-07	1.13E+011	2.53E-001
0	3		6.80E+010	0.00E+000
0	2		1.41E+009	6.70E-001
0	1		3.30E+008	1.46E+000
1	4	1998-03-19	6.28E+010	0.00E+000
1	3		1.93E+009	4.49E-001
1	2		2.87E+008	1.45E+000
1	1		8.38E+006	5.22E+000
2	4	1997-08-28	1.68E+011	0.00E+000
2	3		2.39E+009	4.56E-001
2	2		3.53E+008	1.45E+000
2	1		1.44E+007	4.88E+000
3	4	1996-05-16	1.76E+011	0.00E+000
3	3		1.95E+009	5.11E-001
3	2		7.05E+008	1.34E+000
3	1		8.26E+006	5.12E+000
4	4	1997-03-13	2.77E+011	0.00E+000
4	3		9.73E+009	4.72E-001
4	2		4.68E+008	1.10E+000
4	1		3.81E+007	3.23E+000
5	5	1997-08-15	1.35E+011	0.00E+000
5	4		1.79E+009	6.15E-001
5	3		6.25E+008	1.41E+000
5	2		1.09E+008	2.37E+000
5	1		1.24E+008	5.04E+000
6	5	1998-03-04	2.46E+011	0.00E+000
6	4		2.88E+009	3.77E-001
6	3		4.45E+008	1.11E+000
6	2		4.18E+007	3.20E+000
6	1		1.11E+007	5.70E+000
7	3	1998-03-28	5.40E+010	0.00E+000
7	2		6.44E+008	8.26E-001
7	1		1.09E+007	5.01E+000
8	3	1998-04-26	6.97E+010	0.00E+000
8	2		4.74E+008	9.31E-001
8	1		4.96E+007	5.20E+000
9	3	1999-05-21	1.54E+010	2.40E-001
9	2		2.47E+011	0.00E+000
9	1		4.17E+008	9.80E-001
10	5	2001-03-04	2.97E+009	4.53E-001
10	4		1.59E+011	0.00E+000
10	3		6.97E+008	1.28E+000
10	2		3.64E+007	2.24E+000

Epoch	Component	Date	Brightness Temperature (K)	Core Distance (mas)
10	1		6.16E+006	5.90E+000
11	3	2006-04-05	8.49E+011	0.00E+000
11	2		1.52E+009	4.72E-001
11	1		1.74E+008	1.67E+000
12	4	2006-06-25	7.86E+012	0.00E+000
12	3		2.09E+009	3.10E-001
12	2		2.83E+008	1.08E+000
12	1		1.33E+007	3.77E+000
13	3	2007-02-05	2.52E+011	0.00E+000
13	2		1.07E+009	5.59E-001
13	1		3.84E+007	2.48E+000
14	3	2007-06-03	3.04E+011	0.00E+000
14	2		6.30E+008	7.01E-001
14	1		2.81E+007	3.13E+000
15	3	2007-06-15	2.00E+011	0.00E+000
15	2		7.80E+008	5.79E-001
15	1		4.22E+007	2.67E+000
16	5	2007-09-06	2.50E+011	0.00E+000
16	4		2.70E+009	2.75E-001
16	3		3.82E+008	1.14E+000
16	2		2.60E+007	2.99E+000
16	1		2.20E+006	1.14E+001
17	6	2008-05-01	2.69E+011	0.00E+000
17	5		1.92E+009	3.56E-001
17	4		2.72E+008	1.20E+000
17	3		2.19E+007	3.57E+000
17	2		1.03E+007	6.98E+000
17	1		2.55E+006	1.13E+001
18	3	2008-06-25	1.99E+011	0.00E+000
18	2		8.58E+008	5.82E-001
18	1		2.75E+007	3.07E+000
19	3	2008-07-17	2.91E+011	0.00E+000
19	2		8.14E+008	6.62E-001
19	1		2.67E+007	3.12E+000
20	4	2008-10-03	2.46E+013	0.00E+000
20	3		3.78E+009	1.82E-001
20	2		2.43E+008	1.11E+000
20	1		3.16E+007	3.53E+000
21	4	2009-01-30	2.98E+011	0.00E+000
21	3		2.28E+009	3.57E-001
21	2		2.45E+008	1.34E+000
21	1		2.09E+007	3.98E+000
22	4	2009-04-22	1.89E+011	0.00E+000
22	3		1.77E+009	3.60E-001
22	2		1.73E+008	1.16E+000
22	1		7.75E+006	4.58E+000

Epoch	Component	Date	Brightness Temperature (K)	Core Distance (mas)
23	4	2009-05-02	4.68E+011	0.00E+000
23	3		2.47E+009	3.32E-001
23	2		2.80E+008	1.16E+000
23	1		2.01E+007	3.38E+000
24	3	2009-06-25	3.74E+011	0.00E+000
24	2		5.69E+008	6.76E-001
24	1		1.71E+007	3.06E+000
25	4	2009-12-17	7.79E+011	0.00E+000
25	3		9.64E+008	4.70E-001
25	2		5.83E+010	1.42E+000
25	1		1.72E+007	3.36E+000
26	4	2010-02-11	8.09E+011	0.00E+000
26	3		7.74E+009	3.00E-001
26	2		3.05E+008	8.54E-001
26	1		2.06E+007	3.00E+000
27	3	2010-10-12	1.39E+011	0.00E+000
27	2		7.68E+008	7.53E-001
27	1		2.58E+007	3.63E+000
28	3	2010-10-15	1.65E+011	0.00E+000
28	2		8.40E+008	5.92E-001
28	1		3.67E+007	2.62E+000
29	4	2010-11-29	1.92E+011	0.00E+000
29	3		2.69E+009	3.47E-001
29	2		2.57E+008	1.17E+000
29	1		3.31E+007	3.89E+000
30	3	2011-07-24	1.66E+011	0.00E+000
30	2		4.26E+008	7.63E-001
30	1		1.79E+007	3.91E+000
31	3	2011-12-29	1.21E+011	0.00E+000
31	2		4.44E+008	6.36E-001
31	1		2.79E+007	3.59E+000
32	4	2012-04-29	1.70E+011	0.00E+000
32	3		1.11E+009	4.58E-001
32	2		1.85E+008	1.44E+000
32	1		1.19E+007	4.06E+000
33	3	2012-12-10	1.50E+011	0.00E+000
33	2		1.35E+009	5.96E-001
33	1		5.86E+007	2.07E+000
34	4	2012-12-23	4.03E+011	0.00E+000
34	3		2.44E+009	5.20E-001
34	2		4.23E+008	1.46E+000
34	1		1.76E+007	3.51E+000

Epoch	Component	Date	Brightness Temperature (K)	Core Distance (mas)
35	4	2013-01-21	4.92E+011	0.00E+000
35	3		3.37E+009	3.71E-001
35	2		4.22E+008	1.34E+000
35	1		2.28E+007	3.51E+000
36	4	2013-02-10	6.75E+011	0.00E+000
36	3		2.52E+009	4.08E-001
36	2		3.05E+008	1.38E+000
36	1		2.53E+007	3.44E+000
37	4	2013-05-05	1.25E+012	0.00E+000
37	3		2.47E+009	4.22E-001
37	2		2.88E+008	1.23E+000
37	1		3.10E+007	3.56E+000
38	4	2013-07-08	3.21E+011	0.00E+000
38	3		3.06E+009	3.57E-001
38	2		4.47E+008	1.22E+000
38	1		2.61E+007	3.70E+000
39	4	2013-07-30	4.67E+011	0.00E+000
39	3		2.75E+009	3.94E-001
39	2		3.35E+008	1.36E+000
39	1		2.76E+007	3.57E+000
40	4	2013-08-20	3.28E+011	0.00E+000
40	3		2.83E+009	4.33E-001
40	2		4.00E+008	1.31E+000
40	1		3.81E+007	2.87E+000

TABLE A.4: 0106+013; Each epoch with the corresponding component is listed; the date is given as yyyy-mm-dd; the brightness temperature and the core distance for each component is listed.

Epoch	Component	Date	Brightness Temperature (K)	Core Distance (mas)
0	3	1998-03-19	7.78E+011	0.00E+000
0	2		3.96E+010	2.60E-001
0	1		8.25E+008	1.42E+000
1	5	1997-08-28	1.69E+012	0.00E+000
1	4		8.52E+010	3.37E-001
1	3		6.19E+009	9.60E-001
1	2		2.20E+009	1.83E+000
1	1		3.91E+008	2.43E+000
2	4	1999-05-21	2.88E+012	0.00E+000
2	3		7.84E+010	4.03E-001
2	2		3.72E+009	7.81E-001
2	1		5.44E+008	2.24E+000
3	4	2001-01-21	1.18E+012	0.00E+000
3	3		4.28E+010	3.47E-001
3	2		3.14E+009	8.24E-001
3	1		4.33E+008	1.77E+000
4	6	2002-10-20	1.60E+012	0.00E+000
4	5		5.85E+010	2.66E-001
4	4		1.55E+009	3.11E-001
4	3		1.33E+010	8.92E-001
4	2		1.13E+009	2.01E+000
4	1		1.19E+009	3.37E+000
5	4	2004-09-11	7.96E+011	0.00E+000
5	3		3.34E+010	6.18E-001
5	2		3.62E+009	9.17E-001
5	1		2.53E+008	3.54E+000
6	3	2005-07-24	4.28E+011	0.00E+000
6	2		1.32E+010	8.09E-001
6	1		1.19E+009	1.79E+000
7	5	2006-07-07	8.86E+011	0.00E+000
7	4		1.12E+010	5.35E-001
7	3		6.78E+009	1.14E+000
7	2		2.89E+009	1.93E+000
7	1		3.06E+008	2.82E+000
8	5	2007-06-03	2.40E+012	0.00E+000
8	4		7.06E+009	7.03E-001
8	3		4.51E+009	1.29E+000
8	2		3.36E+009	1.94E+000
8	1		2.17E+008	3.45E+000

---

Epoch	Component	Date	Brightness Temperature (K)	Core Distance (mas)
9	4	2008-11-19	8.63E+012	0.00E+000
9	3		3.07E+009	7.04E-001
9	2		2.31E+009	1.49E+000
9	1		1.84E+008	3.55E+000
10	2	2010-09-29	2.35E+012	0.00E+000
10	1		2.54E+009	2.00E+000
10	2		2.35E+012	0.00E+000
10	1		2.54E+009	2.00E+000
11	2	2011-12-12	6.71E+011	0.00E+000
11	1		9.78E+008	2.06E+000
12	2	2012-05-24	3.06E+011	0.00E+000
12	1		1.14E+009	2.49E+000
13	5	2012-22-02	1.87E+013	4.04E-001
13	4		7.65E+011	0.00E+000
13	3		1.33E+011	3.05E-001
13	2		5.94E+008	1.34E+000
13	1		4.21E+008	3.28E+000
14	4	2013-06-02	1.05E+012	0.00E+000
14	3		1.19E+011	7.07E-001
14	2		9.82E+009	9.75E-001
14	1		4.85E+008	1.52E+000

---

TABLE A.5: 0122-003; Each epoch with the corresponding component is listed; the date is given as yyyy-mm-dd; the brightness temperature and the core distance for each component is listed.

Epoch	Component	Date	Brightness Temperature (K)	Core Distance (mas)
0	5	1998-06-05	1.60E+011	0.00E+000
0	4		4.42E+010	2.13E-001
0	3		9.43E+009	1.66E+000
0	2		2.02E+009	3.59E+000
0	1		4.46E+008	6.48E+000
1	4	1998-09-29	3.06E+011	0.00E+000
1	3		7.06E+009	1.61E+000
1	2		2.86E+009	3.58E+000
1	1		4.33E+008	6.42E+000
2	4	1998-12-05	2.68E+011	0.00E+000
2	3		6.92E+009	1.62E+000
2	2		2.03E+009	3.59E+000
2	1		3.43E+008	6.38E+000
3	6	2011-07-15	7.19E+010	0.00E+000
3	5		2.66E+010	4.60E-001
3	4		5.74E+009	1.92E+000
3	3		5.75E+008	3.26E+000
3	2		2.70E+009	4.55E+000
3	1		3.21E+007	6.00E+000
4	6	2012-05-24	7.59E+010	0.00E+000
4	5		1.00E+010	3.67E-001
4	4		6.75E+009	2.06E+000
4	3		6.89E+008	3.44E+000
4	2		1.32E+009	4.70E+000
4	1		1.14E+008	6.78E+000
5	4	2012-11-11	2.57E+011	0.00E+000
5	3		1.36E+010	3.23E-001
5	2		5.07E+009	2.16E+000
5	1		1.14E+009	4.71E+000
6	8	2013-02-28	1.64E+013	0.00E+000
6	7		1.74E+011	3.21E-001
6	6		4.74E+009	8.51E-001
6	5		1.48E+009	1.85E+000
6	4		8.66E+009	2.28E+000
6	3		7.17E+008	3.46E+000
6	2		1.40E+009	4.85E+000
6	1		6.72E+007	5.87E+000

TABLE A.6: 1652+398; Each epoch with the corresponding component is listed; the date is given as yyyy-mm-dd; the brightness temperature and the core distance for each component is listed.

Epoch	Component	Date	Brightness Temperature (K)	Core Distance (mas)
0	10	1995-04-07	1.67E+008	1.02E+001
0	9		5.99E+008	7.09E+000
0	8		3.13E+007	7.30E+000
0	7		6.65E+007	4.03E+000
0	6		3.17E+008	2.75E+000
0	5		3.32E+008	2.65E+000
0	4		3.15E+008	1.64E+000
0	3		1.07E+009	5.92E-001
0	2		2.13E+011	3.15E-001
0	1		2.97E+009	0.00E+000
1	10	1996-07-10	4.42E+008	1.08E+001
1	9		1.14E+008	9.56E+000
1	8		7.88E+007	8.61E+000
1	7		1.66E+008	7.96E+000
1	6		9.36E+007	6.96E+000
1	5		7.30E+007	4.39E+000
1	4		2.59E+008	2.87E+000
1	3		4.17E+008	1.37E+000
1	2		1.77E+009	4.94E-001
1	1		1.14E+011	0.00E+000
2	9	1995-12-15	1.42E+008	1.07E+001
2	8		2.62E+008	7.38E+000
2	7		1.34E+008	7.82E+000
2	6		3.99E+007	7.20E+000
2	5		1.20E+008	4.07E+000
2	4		3.24E+008	2.62E+000
2	3		9.90E+008	9.08E-001
2	2		3.48E+009	3.20E-001
2	1		1.48E+011	0.00E+000
3	8	1998-10-30	2.81E+008	8.07E+000
3	7		3.73E+008	7.44E+000
3	6		5.36E+007	7.82E+000
3	5		6.63E+008	8.43E+000
3	4		6.17E+007	4.41E+000
3	3		2.91E+008	2.41E+000
3	2		2.18E+009	3.75E-001
3	1		1.28E+011	0.00E+000
4	7	1995-01-20	1.56E+008	6.79E+000
4	6		2.05E+008	5.16E+000
4	5		2.08E+008	2.96E+000
4	4		5.36E+008	1.22E+000
4	3		2.42E+009	6.41E-001

Epoch	Component	Date	Brightness Temperature (K)	Core Distance (mas)
4	2		5.39E+011	0.00E+000
4	1		4.43E+009	4.61E-001
5	7	1996-05-16	2.94E+008	8.92E+000
5	6		1.07E+008	7.76E+000
5	5		1.24E+009	5.63E+000
5	4		1.58E+008	4.22E+000
5	3		2.56E+008	2.54E+000
5	2		1.89E+009	5.73E-001
5	1		2.77E+011	0.00E+000
6	8	1997-02-09	2.72E+008	7.81E+000
6	7		4.84E+007	7.56E+000
6	6		1.45E+008	4.16E+000
6	5		1.39E+009	3.51E+000
6	4		2.83E+008	2.61E+000
6	3		2.07E+009	2.95E+000
6	2		1.39E+009	5.78E-001
6	1		1.29E+011	0.00E+000
7	8	1997-03-13	4.38E+008	7.83E+000
7	7		5.30E+007	7.60E+000
7	6		1.99E+008	3.88E+000
7	5		1.13E+009	3.74E+000
7	4		3.16E+008	2.65E+000
7	3		1.07E+009	8.57E-001
7	2		2.10E+011	0.00E+000
7	1		3.21E+009	3.12E-001
8	9	1997-05-26	1.78E+008	7.88E+000
8	8		4.33E+007	7.67E+000
8	7		2.49E+008	3.99E+000
8	6		1.77E+008	4.28E+000
8	5		4.99E+008	4.23E+000
8	4		9.19E+008	3.50E+000
8	3		2.99E+008	2.38E+000
8	2		1.45E+009	6.08E-001
8	1		1.42E+011	0.00E+000
9	7	1997-08-15	4.98E+007	7.42E+000
9	6		3.39E+008	4.39E+000
9	5		1.26E+009	3.57E+000
9	4		3.53E+008	2.52E+000
9	3		7.50E+008	8.80E-001
9	2		1.69E+009	2.97E-001
9	1		1.62E+011	0.00E+000

Epoch	Component	Date	Brightness Temperature (K)	Core Distance (mas)
10	11	1998-03-04	1.73E+008	7.43E+000
10	10		2.67E+007	7.86E+000
10	9		9.00E+007	6.47E+000
10	8		1.68E+008	4.96E+000
10	7		1.39E+008	4.07E+000
10	6		4.78E+011	3.54E+000
10	5		4.23E+008	2.23E+000
10	4		3.09E+008	2.98E+000
10	3		1.08E+009	8.26E-001
10	2		1.42E+010	1.99E-001
10	1		2.77E+011	0.00E+000
11	8	1998-03-28	2.02E+008	7.37E+000
11	7		8.78E+007	5.34E+000
11	6		6.44E+007	6.06E+000
11	5		1.60E+008	4.61E+000
11	4		3.00E+008	2.78E+000
11	3		5.44E+008	1.61E+000
11	2		1.26E+009	5.67E-001
11	1		1.29E+011	0.00E+000
12	10	1998-04-26	2.15E+008	7.24E+000
12	9		7.47E+007	7.29E+000
12	8		1.18E+008	6.61E+000
12	7		8.85E+007	5.07E+000
12	6		1.56E+008	4.40E+000
12	5		2.55E+008	3.46E+000
12	4		2.51E+008	2.53E+000
12	3		8.19E+008	9.11E-001
12	2		3.08E+009	3.27E-001
12	1		1.85E+011	0.00E+000
13	9	1998-05-15	4.01E+006	1.19E+001
13	8		2.18E+008	7.35E+000
13	7		8.73E+007	7.45E+000
13	6		1.50E+008	6.85E+000
13	5		1.23E+008	4.70E+000
13	4		2.56E+008	3.11E+000
13	3		2.47E+008	1.65E+000
13	2		1.62E+009	5.97E-001
13	1		1.15E+011	0.00E+000
14	6	1999-07-19	3.08E+007	1.00E+001
14	5		1.55E+008	7.69E+000
14	4		1.65E+008	3.41E+000
14	3		2.31E+008	1.87E+000
14	2		1.63E+009	7.45E-001
14	1		1.17E+011	0.00E+000

Epoch	Component	Date	Brightness Temperature (K)	Core Distance (mas)
15	6	2001-12-30	2.29E+007	8.04E+000
15	5		4.47E+007	4.99E+000
15	4		2.71E+008	3.06E+000
15	3		6.93E+008	1.05E+000
15	2		3.90E+009	3.04E-001
15	1		3.87E+011	0.00E+000
16	6	2002-12-13	3.66E+007	7.46E+000
16	5		1.06E+008	5.27E+000
16	4		2.25E+008	3.43E+000
16	3		3.30E+008	1.85E+000
16	2		1.90E+009	3.99E-001
16	1		2.07E+011	0.00E+000
17	7	2003-08-22	1.54E+008	8.38E+000
17	6		6.46E+008	7.65E+000
17	5		4.50E+007	5.46E+000
17	4		1.99E+008	3.00E+000
17	3		7.95E+008	1.22E+000
17	2		2.02E+009	5.73E-001
17	1		1.31E+011	0.00E+000
18	10	2003-08-23	6.85E+007	1.04E+001
18	9		6.19E+007	7.99E+000
18	8		3.81E+008	8.44E+000
18	7		2.35E+008	8.11E+000
18	6		4.32E+007	6.35E+000
18	5		3.00E+008	2.92E+000
18	4		1.59E+008	2.87E+000
18	3		7.05E+008	1.25E+000
18	2		2.86E+009	6.29E-001
18	1		1.49E+011	0.00E+000
19	10	2003-09-26	2.96E+007	8.31E+000
19	9		1.81E+008	8.56E+000
19	8		3.54E+008	7.98E+000
19	7		4.57E+008	6.97E+000
19	6		3.79E+007	4.81E+000
19	5		2.08E+008	3.06E+000
19	4		1.79E+008	2.78E+000
19	3		6.73E+008	1.21E+000
19	2		1.96E+009	5.90E-001
19	1		1.31E+011	0.00E+000
20	7	2004-05-29	1.84E+007	1.15E+001
20	6		6.03E+007	8.13E+000
20	5		5.78E+007	5.32E+000
20	4		2.04E+008	2.98E+000
20	3		5.28E+008	1.31E+000
20	2		2.20E+009	6.38E-001
20	1		1.26E+011	0.00E+000

Epoch	Component	Date	Brightness Temperature (K)	Core Distance (mas)
21	7	2006-02-12	2.41E+007	9.52E+000
21	6		8.35E+007	8.78E+000
21	5		4.59E+007	5.27E+000
21	4		3.07E+008	2.64E+000
21	3		9.13E+008	1.08E+000
21	2		3.81E+009	1.90E-001
21	1		1.69E+011	0.00E+000
22	8	2007-01-06	3.38E+007	8.11E+000
22	7		4.07E+007	5.71E+000
22	6		1.03E+008	4.74E+000
22	5		3.99E+008	2.83E+000
22	4		3.59E+008	1.72E+000
22	3		1.77E+009	1.11E+000
22	2		2.60E+009	5.00E-001
22	1		1.01E+011	0.00E+000
23	7	2007-03-28	3.87E+007	8.17E+000
23	6		5.68E+007	5.94E+000
23	5		1.41E+008	4.95E+000
23	4		2.73E+008	2.72E+000
23	3		9.39E+008	1.11E+000
23	2		3.82E+009	3.76E-001
23	1		1.83E+011	0.00E+000
24	7	2007-06-10	4.18E+007	8.27E+000
24	6		4.44E+007	7.75E+000
24	5		6.27E+007	5.45E+000
24	4		2.76E+008	2.65E+000
24	3		1.07E+009	1.11E+000
24	2		2.91E+009	2.76E-001
24	1		1.19E+011	0.00E+000
25	7	2007-08-16	3.71E+007	8.26E+000
25	6		5.00E+007	5.49E+000
25	5		2.85E+008	2.78E+000
25	4		5.55E+008	1.44E+000
25	3		2.22E+009	1.00E+000
25	2		3.73E+009	3.97E-001
25	1		1.13E+011	0.00E+000
26	6	2008-05-01	4.59E+007	8.46E+000
26	5		3.70E+007	5.64E+000
26	4		2.18E+008	2.88E+000
26	3		8.61E+008	1.08E+000
26	2		3.40E+009	3.29E-001
26	1		2.00E+011	0.00E+000

Epoch	Component	Date	Brightness Temperature (K)	Core Distance (mas)	
27	6	2008-06-25	4.50E+007	8.30E+000	
27	5		4.30E+007	5.30E+000	
27	4		2.35E+008	2.83E+000	
27	3		7.67E+008	1.04E+000	
27	2		1.85E+009	3.46E-001	
27	1		1.16E+011	0.00E+000	
28	6	2009-01-07	9.48E+006	1.10E+001	
28	5		3.68E+007	8.45E+000	
28	4		4.21E+007	5.55E+000	
28	3		2.05E+008	2.80E+000	
28	2		8.34E+008	7.23E-001	
28	1		8.65E+010	0.00E+000	
29	6	2009-05-14	2.89E+007	8.23E+000	
29	5		3.29E+008	2.68E+000	
29	4		1.35E+008	3.61E+000	
29	3		1.29E+009	8.95E-001	
29	2		9.02E+009	3.16E-001	
29	1		1.11E+011	0.00E+000	
30	7		1.78E+007	9.99E+000	
30	6		5.90E+007	6.34E+000	
30	5		1.12E+008	4.89E+000	
30	4		2.01E+008	2.84E+000	
30	3		6.07E+008	1.12E+000	
30	2		2.75E+009	3.72E-001	
30	1		9.48E+010	0.00E+000	
31	9		2011-04-11	1.12E+007	1.69E+001
31	8			2.31E+007	8.37E+000
31	7			2.54E+007	5.49E+000
31	6	1.72E+008		4.24E+000	
31	5	2.28E+008		3.06E+000	
31	4	3.59E+008		1.77E+000	
31	3	6.00E+008		1.18E+000	
31	2	3.11E+009		4.02E-001	
31	1	9.75E+010		0.00E+000	
32	6	2012-03-04		6.73E+006	1.80E+001
32	5		2.66E+007	7.82E+000	
32	4		1.82E+008	2.31E+000	
32	3		6.59E+008	1.08E+000	
32	2		2.15E+009	4.65E-001	
32	1		7.39E+010	0.00E+000	

TABLE A.7: 0333+321; Each epoch with the corresponding component is listed; the date is given as yyyy-mm-dd; the brightness temperature and the core distance for each component is listed.

Epoch	Component	Date	Brightness Temperature (K)	Core Distance (mas)
0	3	1998-03-19	1.07E+009	2.63E+000
0	2		2.85E+009	8.29E-001
0	1		2.06E+011	0.00E+000
1	9	1997-08-28	3.95E+007	1.10E+001
1	8		1.19E+008	8.13E+000
1	7		1.46E+008	5.26E+000
1	6		3.96E+008	5.02E+000
1	5		2.64E+009	2.79E+000
1	4		3.75E+009	2.11E+000
1	3		2.85E+009	9.61E-001
1	2		5.02E+010	5.06E-001
1	1		2.15E+012	0.00E+000
2	5	1995-01-20	6.27E+007	9.65E+000
2	4		2.56E+008	3.23E+000
2	3		1.05E+010	2.22E+000
2	2		2.09E+010	3.95E-001
2	1		5.84E+011	0.00E+000
3	12	1996-05-16	7.92E+007	1.13E+001
3	11		3.55E+008	9.80E+000
3	10		1.05E+009	8.25E+000
3	9		2.28E+008	6.81E+000
3	8		4.69E+008	4.80E+000
3	7		6.31E+008	3.09E+000
3	6		5.42E+009	2.60E+000
3	5		1.37E+010	2.18E+000
3	4		1.07E+009	1.61E+000
3	3		4.58E+009	6.88E-001
3	2		1.76E+011	3.67E-001
3	1		1.51E+012	0.00E+000
4	6	1996-10-27	1.10E+008	6.13E+000
4	5		4.99E+008	4.91E+000
4	4		2.96E+009	2.60E+000
4	3		2.82E+009	1.02E+000
4	2		1.76E+011	4.04E-001
4	1		2.99E+012	0.00E+000
5	7	1997-03-13	4.81E+007	1.15E+001
5	6		1.67E+008	6.78E+000
5	5		4.76E+008	4.97E+000
5	4		2.82E+009	2.63E+000
5	3		2.22E+009	1.05E+000
5	2		3.99E+010	4.75E-001
5	1		1.09E+012	0.00E+000

Epoch	Component	Date	Brightness Temperature (K)	Core Distance (mas)
6	4	1999-11-06	5.70E+008	5.43E+000
6	3		1.39E+009	2.89E+000
6	2		1.22E+010	1.02E+000
6	1		2.51E+011	0.00E+000
7	5	2001-03-04	8.34E+007	8.53E+000
7	4		9.51E+008	5.59E+000
7	3		1.04E+009	3.18E+000
7	2		6.12E+009	1.03E+000
7	1		3.97E+011	0.00E+000
8	5	2003-03-29	1.39E+008	6.59E+000
8	4		1.50E+009	5.76E+000
8	3		1.09E+009	3.64E+000
8	2		3.32E+009	1.17E+000
8	1		1.40E+012	0.00E+000
9	7	2004-10-18	5.22E+007	1.15E+001
9	6		1.57E+008	7.03E+000
9	5		1.30E+009	6.05E+000
9	4		4.18E+008	3.84E+000
9	3		2.81E+009	1.94E+000
9	2		4.65E+009	7.65E-001
9	1		2.40E+012	0.00E+000
10	6	2005-02-29	1.01E+008	1.04E+001
10	5		9.97E+008	6.22E+000
10	4		2.81E+008	5.11E+000
10	3		4.33E+010	5.52E+000
10	2		2.96E+009	9.55E-001
10	1		1.35E+012	0.00E+000
11	5	2005-09-23	1.19E+008	9.27E+000
11	4		1.14E+009	6.18E+000
11	3		5.52E+008	4.09E+000
11	2		2.77E+009	1.08E+000
11	1		8.27E+011	0.00E+000
12	7	2005-10-29	9.15E+007	8.59E+000
12	6		1.14E+009	6.28E+000
12	5		4.47E+008	4.24E+000
12	4		1.99E+009	1.40E+000
12	3		2.41E+009	1.06E+000
12	2		9.80E+012	1.90E-001
12	1		1.77E+012	0.00E+000
13	5	2006-07-07	1.28E+008	9.35E+000
13	4		9.81E+008	6.27E+000
13	3		2.95E+008	4.22E+000
13	2		2.90E+009	1.03E+000
13	1		3.80E+011	0.00E+000

Epoch	Component	Date	Brightness Temperature (K)	Core Distance (mas)
14	7	2007-08-09	7.58E+007	8.56E+000
14	6		9.94E+008	6.64E+000
14	5		2.85E+008	4.97E+000
14	4		1.71E+009	2.40E+000
14	3		8.06E+009	1.41E+000
14	2		7.36E+010	4.82E-001
14	1		5.10E+011	0.00E+000
15	6	2009-03-25	4.76E+007	9.68E+000
15	5		7.73E+008	6.85E+000
15	4		3.25E+008	5.11E+000
15	3		7.52E+008	2.91E+000
15	2		6.45E+009	1.19E+000
15	1		1.54E+012	0.00E+000
16	5	2009-08-21	5.91E+007	1.02E+001
16	4		6.16E+008	6.49E+000
16	3		3.56E+008	2.96E+000
16	2		4.64E+009	1.31E+000
16	1		2.14E+012	0.00E+000
17	4	2009-09-15	5.36E+008	6.38E+000
17	3		4.53E+009	1.43E+000
17	2		1.40E+010	9.11E-001
17	1		1.13E+012	0.00E+000
18	5	2009-10-15	9.20E+007	1.02E+001
18	4		6.38E+008	6.39E+000
18	3		6.91E+009	1.40E+000
18	2		4.08E+009	1.27E+000
18	1		1.64E+012	0.00E+000
19	6	2010-08-27	1.20E+008	8.89E+000
19	5		5.93E+008	6.35E+000
19	4		5.59E+008	3.07E+000
19	3		4.65E+009	1.76E+000
19	2		9.26E+009	1.10E+000
19	1		3.45E+012	0.00E+000
20	6	2011-09-12	2.97E+007	1.04E+001
20	5		5.88E+008	6.37E+000
20	4		1.08E+009	3.18E+000
20	3		4.75E+009	1.63E+000
20	2		2.00E+010	1.20E+000
20	1		1.92E+012	0.00E+000
21	6	2012-09-02	5.75E+007	1.00E+001
21	5		5.67E+008	6.36E+000
21	4		3.96E+008	2.61E+000
21	3		6.63E+009	1.60E+000
21	2		7.51E+010	1.25E+000
21	1		6.98E+011	0.00E+000

---

Epoch	Component	Date	Brightness Temperature (K)	Core Distance (mas)
22	3	2013-03-31	3.67E+008	6.26E+000
22	2		8.09E+009	1.45E+000
22	1		3.36E+011	0.00E+000
23	7	2014-01-25	1.69E+008	7.06E+000
23	6		2.70E+008	6.62E+000
23	5		1.90E+009	5.42E+000
23	4		1.55E+009	1.98E+000
23	3		1.19E+010	1.57E+000
23	2		1.94E+010	5.55E-001
23	1		1.97E+011	0.00E+000

---

TABLE A.8: 0224+671; Each epoch with the corresponding component is listed; the date is given as yyyy-mm-dd; the brightness temperature and the core distance for each component is listed.

Epoch	Component	Date	Brightness Temperature (K)	Core Distance (mas)
0	4	1995-01-20	1.74E+009	9.92E-001
0	3		1.25E+011	4.22E-001
0	2		8.02E+012	0.00E+000
0	1		1.03E+008	4.76E+000
1	2	2002-11-23	5.77E+010	0.00E+000
1	1		8.55E+007	7.94E+000
2	6	2004-04-10	1.34E+010	9.55E-001
2	5		8.95E+009	6.17E-001
2	4		5.30E+011	0.00E+000
2	3		1.78E+009	1.32E+000
2	2		1.85E+007	6.50E+000
2	1		5.73E+007	8.66E+000
3	4	2005-04-21	6.21E+008	1.63E+000
3	3		1.11E+010	6.94E-001
3	2		1.51E+011	0.00E+000
3	1		3.90E+007	8.46E+000
4	7	2005-09-05	5.20E+009	7.96E-001
4	6		5.26E+008	1.97E+000
4	5		1.22E+011	3.82E-001
4	4		1.79E+012	0.00E+000
4	3		3.65E+007	4.06E+000
4	2		5.09E+007	9.70E+000
4	1		3.03E+007	7.41E+000
5	4	2005-11-07	5.25E+008	1.80E+000
5	3		3.47E+010	4.38E-001
5	2		8.78E+011	0.00E+000
5	1		3.84E+007	8.71E+000
6	6	2006-10-06	7.76E+008	2.34E+000
6	5		1.39E+010	5.72E-001
6	4		2.12E+011	0.00E+000
6	3		1.19E+008	2.53E+000
6	2		1.83E+007	5.78E+000
6	1		3.31E+007	9.38E+000
7	5	2007-04-18	1.27E+009	2.24E+000
7	4		5.77E+010	0.00E+000
7	3		2.40E+025	3.38E-001
7	2		6.86E+007	2.18E+000
7	1		3.41E+007	8.76E+000

Epoch	Component	Date	Brightness Temperature (K)	Core Distance (mas)
8	6	2007-08-09	4.30E+009	2.54E+000
8	5		7.55E+008	1.39E+000
8	4		3.45E+010	4.97E-001
8	3		8.58E+011	0.00E+000
8	2		3.82E+008	2.98E+000
8	1		3.34E+007	9.17E+000
9	5	2008-06-25	8.74E+008	3.07E+000
9	4		4.56E+010	5.31E-001
9	3		4.67E+011	0.00E+000
9	2		1.08E+008	1.66E+000
9	1		2.56E+007	9.63E+000
10	5	2009-01-07	6.32E+008	3.24E+000
10	4		2.28E+010	5.74E-001
10	3		5.97E+011	0.00E+000
10	2		1.75E+008	2.58E+000
10	1		2.88E+007	9.71E+000
11	5	2009-06-03	4.27E+011	1.15E+000
11	4		4.06E+010	5.04E-001
11	3		1.18E+012	0.00E+000
11	2		4.58E+008	3.41E+000
11	1		2.70E+007	9.86E+000
12	5	2010-01-16	6.82E+010	4.84E-001
12	4		5.40E+008	1.02E+000
12	3		2.55E+012	0.00E+000
12	2		3.66E+008	3.64E+000
12	1		2.49E+007	9.97E+000
13	5	2010-11-04	9.01E+009	6.43E-001
13	4		1.62E+011	1.85E-001
13	3		5.27E+013	0.00E+000
13	2		3.28E+008	4.02E+000
13	1		2.27E+007	1.02E+001
14	7	2011-07-24	4.09E+010	5.95E-001
14	6		1.47E+009	9.70E-001
14	5		4.49E+011	0.00E+000
14	4		2.37E+008	4.10E+000
14	3		2.07E+007	2.09E+000
14	2		2.33E+008	4.53E+000
14	1		2.09E+007	1.03E+001
15	5	2012-03-27	1.34E+008	3.02E+000
15	4		1.61E+010	4.82E-001
15	3		9.31E+011	0.00E+000
15	2		3.90E+008	4.64E+000
15	1		2.14E+007	1.07E+001

---

Epoch	Component	Date	Brightness Temperature (K)	Core Distance (mas)
16	6	2012-11-21	1.21E+009	1.24E+000
16	5		3.33E+010	6.49E-001
16	4		6.09E+011	0.00E+000
16	3		1.18E+008	4.61E+000
16	2		2.77E+008	4.83E+000
16	1		1.86E+007	1.08E+001
17	6	2013-02-10	7.91E+008	1.33E+000
17	5		1.76E+010	6.39E-001
17	4		9.52E+011	0.00E+000
17	3		1.11E+008	4.57E+000
17	2		2.98E+008	4.91E+000
17	1		1.87E+007	1.09E+001
18	6	2013-07-30	5.08E+009	6.56E-001
18	5		4.33E+010	4.78E-001
18	4		1.08E+012	0.00E+000
18	3		2.32E+007	2.87E+000
18	2		2.41E+008	4.96E+000
18	1		1.26E+007	1.03E+001

---